Quantum dots: concept and application for image sensors

Adrián Romero Campelo

SUPERVISORS

Jorge Fernández Berni

Juan Antonio Leñero Bardallo

Bachelor's Thesis

Degree in Physics

Department of Electronics and Electromagnetism

Faculty of Physics

Universidad de Sevilla

June 2021

Abstract

The aim of this Bachelor's Thesis is to introduce the concept of quantum dots and their possible application to photodetection. In the first part of this work (Chapter 2), a general outline of what quantum dots are and how they are manufactured (materials, techniques employed) will be provided. Besides, a complete description of the band structure of quantum dots, with an emphasis on their optoelectronic features, will be given too. In the second part of the thesis (Chapter 3), photodetection technologies are covered. After an introduction to the state of art of image sensors, the latest advances in quantum dot photodetection will be presented, considering their figures of merit and possible adaptation to current available production methods.

Contents

List of Figures **iv**

1 Introduction **1**

2 Quantum Dots **3**

2.1 Epitaxial crystal growth 3

2.2 Strained Heterostructures 4

2.2.1 Self-assembled Structures 5

2.3 Colloidal Quantum Dots 7

2.3.1 Ink-printed QDs 7

2.3.2 Spin-coating 9

2.4 Energy Spectrum of QDs 10

2.4.1 QD Band structure 10

2.4.2 Effects of strain 12

2.4.3 Effects of piezoelectricity 14

2.4.4 Coulomb interaction 16

2.4.5 Optical Properties 17

2.4.6 Mini-band formation 19

2.5 Simulations 20

3 Photodetectors **25**

3.1 State of the Art 25

3.1.1 Visible Spectrum 25

3.1.2 Infrared spectrum 28

3.2 QD Photodetectors 31

3.2.1 PbS Quantum Dot Photodetectors 32

3.2.2 Ge Quantum Dot Photodetectors 41

4 Conclusions **44**

A Image Sensor Parameters **51**

B Image Sensor Technologies **53**

B.0.1 Charge Coupled Devices (CCDs) 53

B.0.2 Complementary-Metal-Oxide-Semiconductor (CMOS) 53

List of Figures

2.1 Types of bonding between substrate and overlayer [37]. 4
2.2 Nucleation process of Ge quantum dots grown in Si_3N_4 [39]. 6
2.3 Quantum dots of different sizes, starting at 13 nm up to 90 nm [39]. 7
2.4 QD printing process: a nozzle releases droplets containing CQD and deposited on a layer [35]. 8
2.5 Microscope and AFM analysis of a printed QD using as ligands a) NMP, b) BTA:NMP, c) BTA:NMP on a substrate heated at 60°C. the latest one shows the most uniform results and smallest roughness [35]. 8
2.6 Process involved in spin coating, including: deposition, spin-up, spin-off and evaporation [31]. 9
2.7 Energy diagram comparison between the cases without/with strain included in the model. A: $x_{As} = 0.2, y_{As} = 0.2$; B: $x_{As} = 0.8, y_{As} = 0.8$; C: $x_{As} = 0.8, y_{As} = 0.8$; A: $x_{As} = 0.2, y_{As} = 0.8$. A notable shift in the levels can be observed [16]. 15
2.8 Absorption coefficient for a InAs/GaAs QD with base width 124$\mathring{A}$ and height 62$\mathring{A}$.The plane polarization is absorbed much more efficiently than the z-polarization [12]. 18
2.9 a) Mini-band as a function of the interdot distance. b) Mini-band as a function of size (for H=15nm) [21]. 19
2.10 Quantum Dot Lab interface. 20
2.11 Absorption spectrum of the Ge QDs (I). 21
2.12 Comparison of the absorption spectra for different polarization angles (I). . 22
2.13 Energy states (II). 23
2.14 Absorption spectrum of the Ge QDs (II). 23
2.15 Comparison of the absorption spectra for different polarization angles (II). 24

3.1 Simplified diagram showing the absorption and emission processes in a semiconductor [27]. 26
3.2 Diagram of an standard silicon photodiode [18]. 27
3.3 Cross section of a photogate [18]. 27
3.4 CMOS image sensor, layer by layer [18]. 28
3.5 Current IR spectrum and its imaging standard ranges [36]. 29
3.6 Cross section of a typical IR sensor [28]. 30
3.7 Schematic comparison of EQE between silicon, InGaAs and PbS QDs [23]. 32
3.8 Absorption peak depending on dot size [23]. 33
3.9 Cross image of the QD stack, obtained using annular bright field scanning transmission electron microscopy [8]. 34
3.10 Cross view of the stack, schematic (left) and obtained by transmission electron microscopy [23]. 34
3.11 Photodetector with circuit diagram, includind the TMDC layer [26]. 34
3.12 Scanning electron microscopy representing the full QD stack [35]. 35
3.13 EQE comparison for different bias voltages and wavelengths [35]. 36
3.14 Transient photoresponse [23]. 37
3.15 Transient photoresponse [8]. 37
3.16 Relaxation times [26]. 37
3.17 Deposition of QD layer [10]. 38
3.18 QDs islands obtained with photolithography techniques [10]. 38
3.19 Packaging of the sensor (left) and cross-section scheme of the photodetector (right) [8]. 39
3.20 Responsivity comparison of three configurations of QD detectors (left) and diagram of the dual stack multispectral QDPD (right) [17]. 40
3.21 Schematic figure of a hybrid multispectral sensor, composed by a Si pixel and a QDPD [8]. 40
3.22 Schematic view of a Ge QDPD on a silicon substrate [5]. 42
3.23 Schematic view of a Ge QDPD on a silicon substrate [32]. 42
3.24 Responsivity and IQE depending on the wavelength 43

4.1 Image through a maritime rain event. Picture taken with the *Acuros CQD 640/640L GigE SWIR Camera* [36]. 45

4.2 Pharmaceutical via labels. Picture taken with the *Acuros CQD 640/640L GigE SWIR Camera* [36]. 45

B.1 Diagram of CCD image sensor [18]. 54

B.2 Potential profile, ilustrating the action of the transfer gate (TG) [7]. 54

Acronyms

CCD Charge Coupled Device.

CMOS Complementary Metal Oxide Semiconductor.

CQD Colloidal Quantum Dots.

EQE External Quantum Efficiency.

IQE Internal Quantum Efficiency.

ITO Indium Tin Oxide.

LWIR Long Wave Infrared.

MBE Molecular Beam Epitaxy.

MOCVD Metal Organic Chemical Vapor Deposition.

MWIR Medium Wave Infrared.

NIR Near-Infrared.

QD Quantum Dot.

QDPD Quantum Dot Photodetector.

QDs Quantum Dots.

SWIR Short Wave Infrared.

TMDC Transition Metal Dichalcogenide.

Chapter 1

Introduction

Obtaining fixed and lasting pictures has been a major concern since the dawn of the earliest civilizations, beginning with pictorial techniques and advancing towards more sophisticated methods. The great steps forward in the field of treatment of the light (e.g., the dark chamber) brought the wish of, not only to interpret, but also to reliably capture what the eye was able to see, and store it permanently. As a result, in the 19th century the first photographs (and cameras, therefore) were taken, as well as their predecessors, *heliography* and *daguerreotype*. The technological breakthrough behind both was based in the use of chemical substances, namely silver nitrate or silver chloride, to capture the image formed by a set of lenses. More accurate and cheaper techniques were developed, but always based in analogue processes. The next revolution on this field would arrive with the advent of solid-state image sensors, which appeared parallel to the development of electronics in the second half of the 20th century.

The era of digital photography also brought a well known term nowadays, the pixel. Without going into much detail, they are the constituent parts or *tiles* a picture can be split up to. Each of these pixels are, in fact, the sensors that react and interpret the incoming light. The two most common underlying technologies of image sensors are the Charge Coupled Device (CCD), and the Complementary Metal Oxide Semiconductor (CMOS) (see Appendix B for more information).

The use of CCDs prevailed over CMOSs, due to their higher performance, specially its clearly lower Fixed Pattern Noise (FPN), defined as "the spacial variation of the sensor response to a uniform input after all the temporal noise has been removed" [18]

CMOS sensors were a hot research topic throughout the last decades of the 20th century, but they would only displace CCDs with the advent of the smartphones, and the strict size and cost requirements for their cameras. Nowadays, CMOSs sensors are the benchmark for image sensing, and can be found in smartphone's cameras, surveillance systems, professional cameras, etc. It is estimated that their share in the sensors market sales is of 89%, what makes its economic interest unquestionable [11]. Besides, a compound annual growth rate of 5.7% in their demand is expected until 2025 [6].

In this search of better and cheaper technologies we find the Quantum Dots (QDs). On a first approach, they consist in nanometric structures, with electric and optical properties of a 0-dimension body. One of these features, that makes them interesting for photodetection, is their absorption and emission tunability to almost any wavelength, achieving a very precise the identification of the incident light. The opposite effect, emission, has already become mainstream in the manufacture of televisions, with outstanding results [29].

Although CMOSs sensors have achieved a remarkable performance, they still struggle in extreme situations, such as excessive or very low light scenes. To overcome these limitations and others that will be presented in Chapter 3, QD technologies are being developed by many research groups [26][22][8]. Particularly, QD-based photodetection for low-light scenes is one of the hottest research topic of these devices, since they've shown great results in the infrared range [1].

The first part of this Bachelor's Thesis is devoted to provide a complete physical description of QDs, including electronic and optical characteristic, as well as how they are manufactured. Simulations of the theoretical properties explained will be presented. In the second part, current state of the art of CMOSs sensors and how QDs can be implemented for photodetection will be covered in detail.

[1] A IR QD based camera has been already commercialized by *SWIR Vision Systems*

Chapter 2

Quantum Dots

Quantum Dots are crystalline structures of nanometric size, with properties changing from those of the bulk crystal, mainly the density of states (0-D instead of 3-D) and electronic states. Next sections will provide a description of QDs' state of the art, covering both how they are grown and their optoelectronic properties. An accurate description of QDs' features is fundamental to implement them in new technologies, so this chapter will be the basis to understand the implementation of a Quantum Dot Photodetector (QDPD) in Chapter 3.

2.1 Epitaxial crystal growth

The first step in the manufacturing of any active device is to grow the bulk crystal, that will be used as substrate of the next layers. This is achieved in standard industrial processes with the *Czochralski Technique* (CZ), which allows to produce high quality polycrystalline materials for semiconductors such as Si, GaAs and InP [34]. Once the bulk crystal is grown, wafers around 250 μm are sliced [1], polished and used for growth of epitaxial layers.

The two main epitaxial growth techniques are Molecular Beam Epitaxy (MBE) and Metal Organic Chemical Vapor Deposition (MOCVD). A detailed explanation of both processes can be found in [34].

[1] The thickness of the wafers may vary depending on their use, from 250 μm up to 675 μm [33].

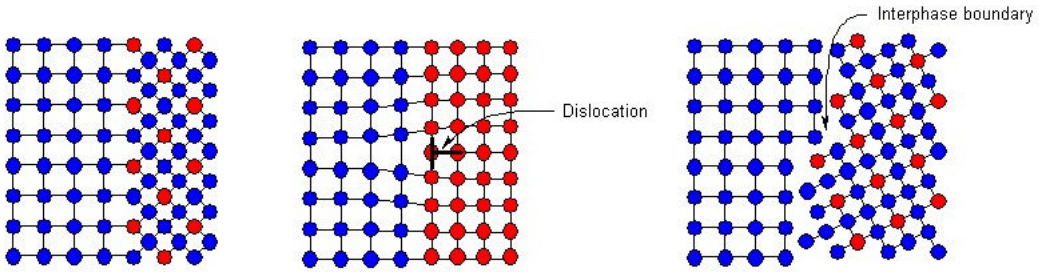

Figure 2.1: Types of bonding between substrate and overlayer [37].

2.2 Strained Heterostructures

To achieve carrier confinement inside the dot, in general a smaller bandgap material has to be embedded within a larger bandgap material, although different configurations are possible. This causes a problem of lattice mismatch between different materials, which can be, however, overcome or even used in favour of the optoelectronic performance.

In epitaxial processes, the overlayer grown on the substrate can have different lattice constants; such epitaxy is called strained epitaxy. If the overlayer is very thin, it has built-in strain and hence the optoelectronic properties are affected. If the substrate and overlayer lattice constants are respectively a_s, a_l, the strain is defined as:

$$\epsilon = \frac{a_s - a_l}{a_l} \tag{2.1}$$

Eq.(2.1) gives a value of the mismatch between two materials. It is simple to check that after $1/\epsilon$ bonds either a missing or extra bond appears: such defects are called dislocations. They are named incoherent structures, and they cost energy to the system.

There is another way for the system to rearrange its bonds, namely a coherent structure. In such cases, substrate and overlayer are almost perfectly bonded by adjusting the lattice constants, causing the overlayer to be under strain. Thus, the system now has a certain strain energy and the band diagram of the semiconductor is altered (see Fig. 2.1). For small lattice mismatch ($\epsilon < 0.1$), overlayer and substrate fit perfectly. However, as the thickness of the overlayer increases, dislocations will eventually be favorable in terms of energy. For example, a surface thickness of $a_s = 10$ nm was reported to yield the lowest dislocation density, for an InAs/GaAsSb system [15].

2.2.1 Self-assembled Structures

Strain energy competes against the chemical bonding energy created by bond formation, as well as the surface effects and the ability of the system to evolve to the minimum free energy. Self-assembled structures have been reported for a wide variety of semiconductor pairs, namely Si/Ge, InAs/GaAs, CdSe/ZnSe, InGaN/GaN, (InGa)(AsSb)/GaAs/GaP, etc [16][3].The main factors affecting the growth are the substrate and deposited material free energies (γ_1, γ_2 respectively) and the interface energy γ_{12}. The material's free energy is defined as the amount of internal energy available to perform work on the system (the formation of the structure in this case) [2]. Strain energy of the film $\mu_2(t)$ should also be considered,that is, the total amount of energy stored in the formation of the strained structure. In terms of the lattice mismatch and the free energy, three possible growing modes may occur:

1. Frank-van der Merwe growth: it is characterized by a low strain ($\epsilon < 2\%$), which results in an almost perfect growth of layer without dislocations. They show no strain energy profile. For this case, $\gamma_1 > \gamma_2 + \gamma_{12}$.

2. Stranski-Krastonow growth: for intermediate strain values, growth starts with monolayers 'wetting' the surface but changes to 3D island-growth mode, maintaining the coherent structure. Thanks to this process, the total free energy of the system is minimized, and the inequality $\gamma_1 > \gamma_2 + \gamma_{12} + \mu_2(t_c)$ is fulfilled (t_c critical thickness).

3. Volmer-Weber growth: occurs at higher lattice mismatch. In this case, only island growth takes place since the cohesive force between atoms in the overlayer is stronger than the force binding them to the substrate. In this case, $\gamma_1 < \gamma_2 + \gamma_{12}$.

Strain provides a mechanism for island-growth, but does not ensure the regular distribution of the QDs; temperature, flux and total coverage must also be considered. Strain-induced elastic forces are long-range interactions, meaning that QDs interact strongly among them, favouring the "self-organization" [3].

Fabrication of Ge QDs

Any QD growing technique pretending to achieve mass production must first be scalable, precise and repeatable. Current CMOS fabrication technologies can fulfil those three

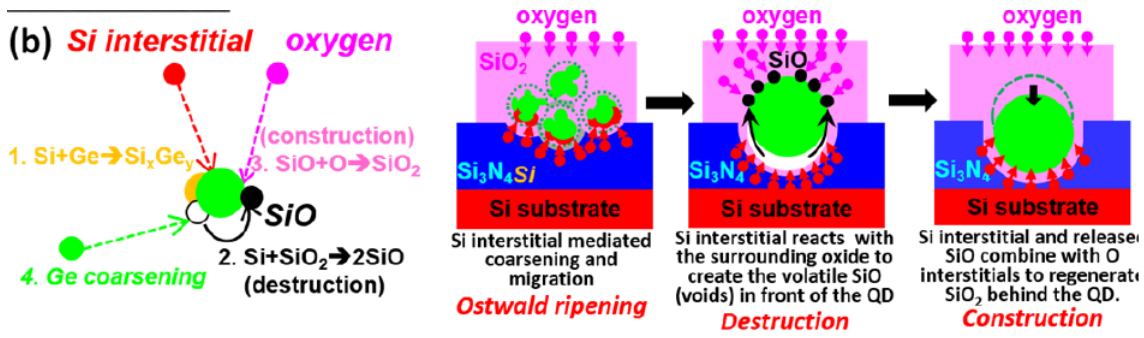

Figure 2.2: Nucleation process of Ge quantum dots grown in Si_3N_4 [39].

requirements, so any new device should preferably adapt to them.A compatible fab process has been recently reported in [39]. In this work Ge QDs with SiO_2 shells were grown on a Si_3N_4 substrate and Ge $QDs/SiO_2/SiGe$ sheets on Si layers.

The dots are created by using selective oxidation of poly $Si_{1-x}Ge_x$ lithographically patterned structures over Si_3N_4 layers; they provide local interstitials for Si, causing the union and migration of the QDs. The process starts with the thermal oxidation (between 850-900 °C) of $Si_{1-x}Ge_x$; Si oxidation is favored over GeO_2, so SiO_2 matrices are formed. Within these matrices, a combination of pure and residual interstitials Ge is found. Then, in a chain reaction, the Ge nanocrystals catalyze the local decomposition and oxidation of Si_3N_4, releasing Si interstitials. This forces nanocrystals to submerge into the substrate, in a process named Ostwald ripening. The Ge QD formation is accompanied with the formation of a 1.5-nm-thick SiO_2 shell.

When the QDs penetrate the Si substrate, it enables the formation of self-aligned heterostructures of Ge QD on the Si surface, providing an array of dots. The resultant dots have a spherical shape, what gives them interesting electronic properties, like 3D bound states (see simulation in Section 2.5). Dots may also be placed precisely: it is achieved via controlled heterogenous nucleation, together with a growth on patterned structures.

The previous features allow to think in future applications for CMOS fabrication, provided that a precise placement of the dots is possible. Besides, the size of the dots is tunable, allowing sizes from 5 nm to 100 nm. This is controlled either with the geometric dimensions or the chemical composition (Ge content in $Si_{1-x}Ge_x$)

2.3 Colloidal Quantum Dots

Colloidal Quantum Dots (CQD) have become, with semiconductor QDs, a hot-research topic in QDs' manufacture, since they offer good electrical and optical properties, while keeping costs of production low [22].

According to the International Union of Pure and Applied Chemistry (IUPAC) a colloid or colloidal is: "a state of subdivision such that the molecules or polymolecular particles dispersed in a medium have at least one dimension between approximately 1 nm and 1 μm, or that in a system, discontinuities are found at distances of that order" [14]. In general, colloids are insoluble particles suspended in a medium.

Regarding the present work, colloidal substances are interesting due to their ability to form quantum dots, by fixing the original liquid substance in a solid structure. Different techniques have been explored to produce CQD: inkjet printed QDs, spin-coating and magnetic sputtering are the most common ones [35][8][23].

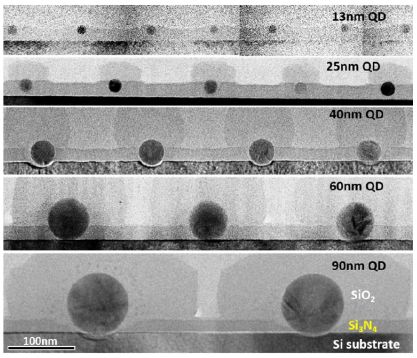

Figure 2.3: Quantum dots of different sizes, starting at 13 nm up to 90 nm [39].

2.3.1 Ink-printed QDs

Inkjet printing has become a promising technology in the manufacture of QDs, due to its speed and easiness compared to other techniques [35]. Basically, a colloidal ink is ejected drop by drop from a nozzle into a substrate and then fixed by some acting ligands. Drops are ejected from the nozzle by applying a pressure pulse in the supply tube. With this process, precise layers of QDs with a homogeneous energy landscape can be deposited. Besides, desired patterns can be accurately reproduced, while reducing material waste.

After the deposition and drying of the colloids, ligands are fundamental in the fixing phase, guaranteeing the stability and electrical conductivity of QDs. Thus, an extensive

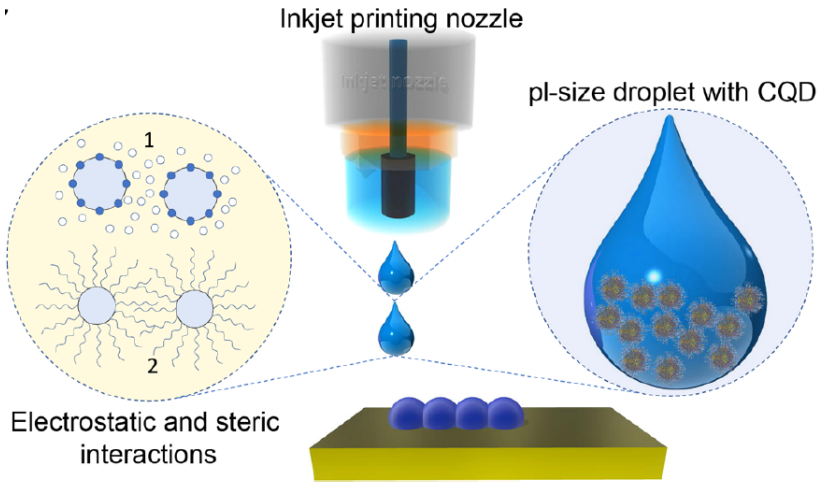

Figure 2.4: QD printing process: a nozzle releases droplets containing CQD and deposited on a layer [35].

research on ligands is in order before printing the dots; otherwise, colloids may suffer surface etching and degradation. In [35], a combination of two ligands, n-butylamine (BTA) and N-methyl-2-pyrrolidone (NMP), in proportion 1:100 respectively, was used. It demonstrated good viscosity, density and surface tension, while maintaining a high boiling point of 202°C. Smooth layers with very low roughness (less than 3.3 nm) have been reported. They have ideal characteristics to apply them in Near Infrared (NIR) image sensors, as will be discussed in Chapter 3.

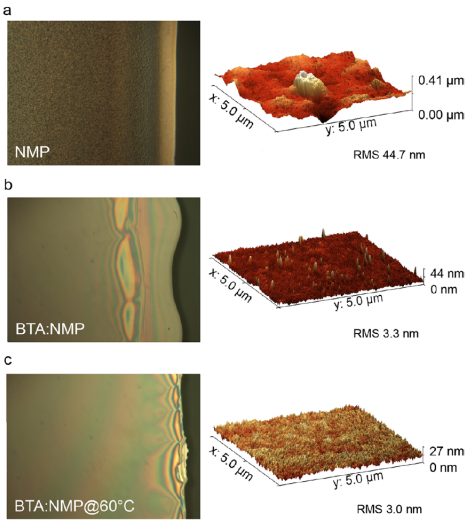

Figure 2.5: Microscope and AFM analysis of a printed QD using as ligands a) NMP, b) BTA:NMP, c) BTA:NMP on a substrate heated at 60°C. the latest one shows the most uniform results and smallest roughness [35].

2.3.2 Spin-coating

Spin coating is the most common technique for depositing layers of QDs [8], [23], as well as in other tasks, such as applying photoresists or any polymer to a surface. It is a batch process, what makes it attention-grabbing to standardize processes. It achieves a solid thin coating on a rigid flat disk or a plate; four stages can be identified in the whole procedure [31]:

1. Deposition: a liquid (the colloidal substance) is deposited onto a substrate at rest or spinning slowly.

2. Spin up: the disc is accelerated to several thousands of revolutions per minute (rpm). Liquid flows radially outwards, spreading the substance to the whole disc; this is caused by the spin up and the consequent centrifugal force. In general, the higher the speed, the thinner the layer. The uniformity in the layer is caused by the balance between centrifugal force and viscosity

3. Spin-off: angular velocity decreases and the excess liquid that covers the substrate flows to the edge of the disc. Thus, the film is thinned almost uniformly.

4. Thinning by evaporation: present volatile components evaporate, leaving a solid layer as result. Afterwards, the surface might be polished to eliminate any possible defect or irregularity.

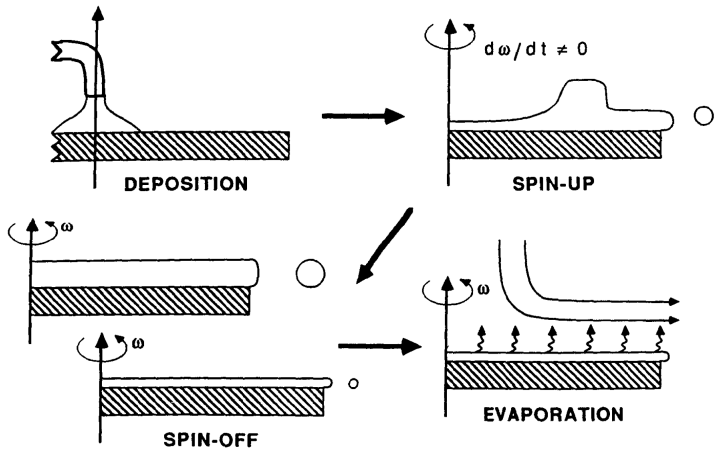

Figure 2.6: Process involved in spin coating, including: deposition, spin-up, spin-off and evaporation [31].

2.4 Energy Spectrum of QDs

Low-dimension systems, like QDs (0-D), show a strong electron confinement, as it has been explained before. In terms of the band structure, that means QDs exhibit an atom-like behavior, with almost discrete energy levels. To prove this important feature, we will address the Schrödinger equation by implementing the widely-used $8k \cdot p$ method.

2.4.1 QD Band structure

In this subsection, the $8k \cdot p$ method for band structure computation will be briefly introduced and applied to the studying case of QD. This approach yields quite accurate results [34] near the band-edges: starting from these zones, perturbative theory is used to describe the bands away from the high-symmetry points. The main advantage of this procedure is that it is capable of obtaining analytic expressions for the band diagrams, which can be adjusted with experimental data. The model will be improved in the following sections by considering the effects of strain, piezoelectricity and Coulomb interaction.

The first step is to solve the time-independent Schrödinger equation (solutions are considered stationary):

$$H\Phi_{n,k} = E_{n,k}\Phi_{n,k} \qquad n = 1, 2, 3... \tag{2.2}$$

where H is the Hamiltonian (not defined yet) and $E_{n,k}$ the energy eigenvalues. The Bloch functions $\Phi_{n,k}$ are the product of a wave function $exp(i\vec{k} \cdot \vec{r})$ and a periodic function $u_{n,k}$:

$$\Phi_{n,k} = exp[i(\vec{k} - \vec{k_0}) \cdot \vec{r}]u_{n,k} \tag{2.3}$$

The total wavefunction for a level n is an expansion of the Bloch functions with the envelope function $F(\vec{k})$ as coefficients:

$$\psi_n = \sum_{n,k} F_n(k)e^{i\vec{k}\vec{r}}u_{n,k} \tag{2.4}$$

Substituting the expression for Bloch's functions Eq.(2.3) and introducing the $8k \cdot p$ method Hamiltonian, the Schrödinger equation reads:

$$\left(\frac{p^2}{2m}+\frac{\hbar\vec{k}\cdot\vec{r}}{m}+\frac{\hbar^2k^2}{2m}+V\right)u_{n,k}=E_{n,k}u_{n,k} \tag{2.5}$$

Equation Eq.(2.5) is much easier to solve than Eq.(2.2), since $u_{n,k}$ is periodic. Usually, k is chosen to be the $\Gamma=[0,0,0]$ point, so (2.5) is simplified to:

$$\left(\frac{p^2}{2m}+V\right)u_{n,0}=E_{n,0}u_{n,0} \tag{2.6}$$

The solutions $u_{n,0}$ form a complete orthonormal set (COS). Once they are known, $\frac{\hbar\vec{k}\cdot\vec{r}}{m}$ and $\frac{\hbar^2k^2}{2m}$ may be treated as perturbations of Eq.(2.6), either with non-degenerate perturbation theory (for the conduction band) or degenerate perturbation theory (valence band).

For non-degenerate bands, the wavefunctions and eigenenergies can be obtained with the following expansions:

$$u_{n,k}=u_{n,0}+\frac{\hbar}{m}\sum_{n'\neq n}\frac{\langle u_{n,0}|\vec{k}\cdot\vec{r}|u_{n',0}\rangle}{E_{n,0}-E_{n',0}}u_{n',0} \tag{2.7}$$

The energy values are respectively:

$$E_{n,k}=E_{n,0}+\frac{\hbar^2k^2}{2m}+\frac{\hbar^2}{m^2}\sum_{n'\neq n}\frac{|\langle u_{n,0}|\vec{k}\cdot\vec{r}|u_{n',0}\rangle|^2}{E_{n,0}-E_{n',0}} \tag{2.8}$$

Focusing now in the degenerate case (valence bands), we find a rather more complicated treatment, where the appearance of two types of carriers (heavy and light holes) that must be considered. The reason of this phenomenon dwells in the coupling of the p-like bands with the spin, which yields a total angular momentum $J=1/2$ for the SO bands and $J=3/2$ for the LH-HH bands [34]. The complete procedure to obtain the energy profile is beyond the scope of this work, so the result proposed by [41] will be taken as valid:

$$E_{hh}=-Ak^2-[B^2k^4+C^2(k_x^2k_y^2+k_y^2k_z^2+k_z^2k_x^2)]^{1/2} \tag{2.9}$$

$$E_{lh}=-Ak^2+[B^2k^4+C^2(k_x^2k_y^2+k_y^2k_z^2+k_z^2k_x^2)]^{1/2} \tag{2.10}$$

A,B,C are related to the Kohn-Luttinger parameters (well known for most semiconductors)

as follows:

$$\begin{aligned} A &= -\left(\frac{\hbar^2}{2m}\right)\gamma_1 \\ B &= -2\left(\frac{\hbar^2}{2m}\right)\gamma_2 \\ \left(\frac{\hbar^2}{2m}\right)\gamma_3 &= \left[\left(B^2/4\right) + \left(C^2/12\right)\right]^{1/2} \end{aligned} \tag{2.11}$$

An interesting property of Eq.(2.9) and Eq.(2.10) that should not be missed is inversion symmetry, $E(k) = E(-k)$, which decreases the degrees of freedom as a consequence of the crystal symmetry. The crystal may not fulfill this property in reality, rather underlies in the chosen Hamiltonian: it is invariant under time reversal (a property of the Hamiltonian for constant energy systems [20]). A Bloch wave travelling with wave vector $\vec{k}$ changes to $-\vec{k}$ under time reversal. Hence, according to the Hamiltonian, the two waves travelling on opposite direction will have the same energy. For $j = 1/2$ band the split-off energy is [41]:

$$E_{SO} = -\Delta_0 + \frac{\hbar^2 k^2}{2m}\left[1 - \frac{2}{3}\left(\frac{P^2}{m(E_0 + \Delta_0)} + \frac{2Q^2}{m(E_0' + \Delta_0)}\right)\right] \tag{2.12}$$

E_0 stands for the energy separation between the Γ_{1c} and $j = 3/2$ bands, whereas E_0' does it for the difference between Γ_{4c} and $j = 3/2$ bands. The parameters P, Q^2 are respectively:

$$\begin{aligned} P &= \frac{2\pi\hbar}{a_0} \\ Q^2 &= \frac{3m^3 E_0 E_0'}{4P^2}\left(\frac{C}{\hbar}\right)^2 \end{aligned} \tag{2.13}$$

a_0 the Bohr radius. The band dispersion for the split-off band is parabolic. The limitation on the accessible energy levels comes from the boundary conditions that restrict the values of the wave vector $\vec{k} = (k_x, k_y, k_z)$.

2.4.2 Effects of strain

The effects of strain must be accounted in a proper model for quantum dots, as its impact in the confinement is comparable to the band gap itself. In this work the approach of a continuum deformation theory proposed in [16] will be followed. This is based in the

strain tensor ϵ:

$$\epsilon = \begin{pmatrix} \epsilon_{xx} & \epsilon_{xy} & \epsilon_{xz} \\ \epsilon_{yx} & \epsilon_{yy} & \epsilon_{yz} \\ \epsilon_{zx} & \epsilon_{zy} & \epsilon_{zz} \end{pmatrix} \tag{2.14}$$

The strain-induced change in the energy profile, for the Γ, L, X points in the conduction band can be approximated as:

$$E_c^i(\widehat{k_0}, \epsilon) = E_c^i(\widehat{k_0}) + a_d^i tr(\epsilon) + a_u^i(\widehat{k_0} \cdot \epsilon \widehat{k_0}) \tag{2.15}$$

where $i \in [\Gamma, L, X]$, a_d^i and a_u^i are the absolute and uniaxial deformation potentials respectively and $tr(\epsilon) = \epsilon_{xx} + \epsilon_{yy} + \epsilon_{zz}$. Evaluating Eq.(2.15) for a simple case when all the strain tensor off-diagonal terms are null, that is, at the vertical center line, one gets:

$$\begin{aligned} E_c^\Gamma([000], \epsilon) &= E_c^\Gamma + a_c^\Gamma tr(\epsilon) \\ E_c^L([111], \epsilon) &= E_c^L + a_c^L tr(\epsilon) + \frac{1}{3} a_{cu}^L tr(\epsilon) \\ E_c^X([100], \epsilon) &= E_c^X + a_c^X tr(\epsilon) + a_{cu}^X(\epsilon_{xx}) \\ E_c^X([010], \epsilon) &= E_c^X + a_c^X tr(\epsilon) + a_{cu}^X(\epsilon_{yy}) \\ E_c^X([001], \epsilon) &= E_c^X + a_c^X tr(\epsilon) + a_{cu}^X(\epsilon_{zz}) \end{aligned} \tag{2.16}$$

As it has been explained before, E_c^i is computed with Eq.(2.8). The values for the deformation potentials depend on the type of QD under study, as well as the bulk material. Worth to mention is the spatial dependence of the high symmetry X point, whereas it is identical for all L-points. This shows not only the complexity of the problem, but also the importance of considering the high symmetry points.

For the valence band, besides heavy, light hole and split-off (or spin-orbit) bands, the coupling between the last two cannot be neglected. Let's define $\delta E = \frac{1}{2} a_u(\epsilon_{xx} + \epsilon_{yy} - 2\epsilon_{zz})$ [16] and Δ_{SO} the spin-orbit splitting. Thus, the expressions for the bands read:

$$\begin{aligned} E_V^{HH}(\Gamma, \epsilon) &= E_V^\Gamma + a_v tr(\epsilon) - \delta E \\ E_V^{LH}(\Gamma, \epsilon) &= E_V^\Gamma + a_v tr(\epsilon) + \frac{1}{2}(\delta E - \Delta_{SO}) + \frac{1}{2}\sqrt{\Delta_{SO}^2 + 2\Delta_{SO}\delta E + 9\delta E^2} \\ E_V^{SO}(\Gamma, \epsilon) &= E_V^\Gamma - \Delta_{SO} + a_v tr(\epsilon) + \frac{1}{2}(\delta E + \Delta_{SO}) - \frac{1}{2}\sqrt{\Delta_{SO}^2 + 2\Delta_{SO}\delta E + 9\delta E^2} \end{aligned} \tag{2.17}$$

Again ,the values E_V^Γ on each case are found using Eq.(2.9), Eq.(2.10) and Eq.(2.12). There is a strong coupling of light-hole and split-off band through the term $2\Delta_{SO}\delta E$, that

can cause a band upshift of at least 100 meV, a remarkable value that shows how this effect cannot be neglected in the calculus of the band diagram. This is also clear in Fig. 2.7, with an upshifht of the confinement energy for all bands higher than 300 meV.

2.4.3 Effects of piezoelectricity

Piezoelectricity is defined as the "generation of electric polarization by the application of stress to a crystal lacking a center of symmetry" [30]. In this section the approach followed is the one proposed in both [1] and [41], which takes into account not only first order component but also the second one. Together with the strain tensor, the polarization is described with an unique parameter (e_{14}) for the linear case and three ($B_{114}, B_{124}, B_{156}$) for the quadratic. The relation is given by:

$$\begin{aligned} p_1 &= 2e_{14} \begin{pmatrix} \epsilon_{yz} \\ \epsilon_{xz} \\ \epsilon_{xy} \end{pmatrix} \\ P_2 &= 2B_{114} \begin{pmatrix} \epsilon xx\epsilon_{yz} \\ \epsilon yy\epsilon_{xz} \\ \epsilon zz\epsilon_{xy} \end{pmatrix} + 2B_{124} \begin{pmatrix} \epsilon_{yz}(\epsilon yy + \epsilon zz) \\ \epsilon_{xz}(\epsilon xx + \epsilon zz) \\ \epsilon_{xy}(\epsilon xx + \epsilon yy) \end{pmatrix} + 4B_{156} \begin{pmatrix} \epsilon_{xz}\epsilon_{xy} \\ \epsilon_{yz}\epsilon_{xy} \\ \epsilon_{yz}\epsilon_{xz} \end{pmatrix} \end{aligned} \tag{2.18}$$

From the polarization $\vec{P} = \vec{P_1} + \vec{P_2}$ we can deduce the piezoelectric charges:

$$\rho_{piezo}(\vec{r}) = -\nabla \vec{P} \tag{2.19}$$

The potential is obtained by solving Poisson's equation, considering the material dependant dielectric constant ($\epsilon_s(\vec{r})$):

$$\rho_p(\vec{r}) = \epsilon_0 \nabla[\epsilon_s(\vec{r}) \nabla V_p(\vec{r})] \tag{2.20}$$

$$\Delta V_p(\vec{r}) = \frac{\rho_p(\vec{r})}{\epsilon_0 \epsilon_s(\vec{r})} - \frac{1}{\epsilon_s(\vec{r})_p} (\vec{r} \cdot \nabla \epsilon_s(\vec{r})) \tag{2.21}$$

The quadratic term should not be in any case neglected, because for large strain it may even dominate over the linear term [30].

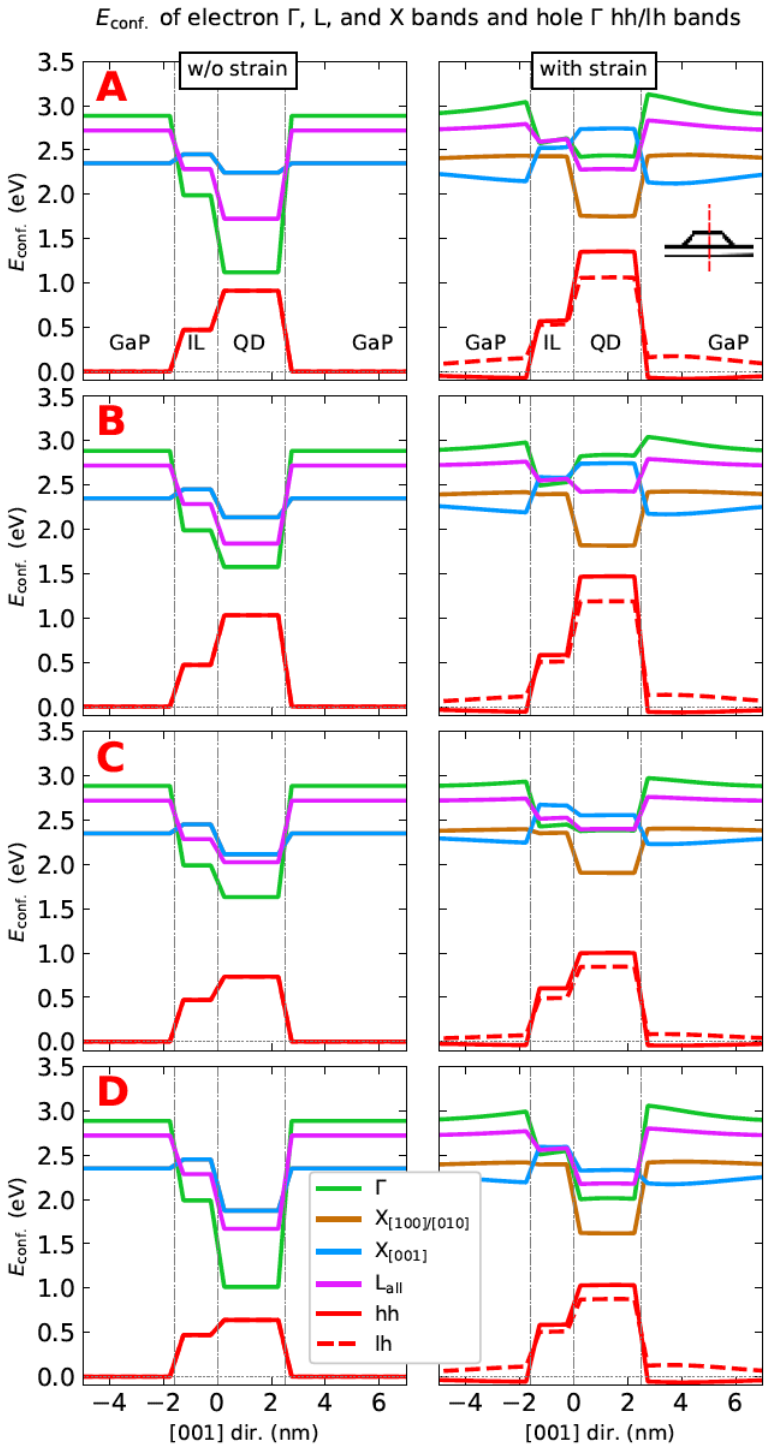

Figure 2.7: Energy diagram comparison between the cases without/with strain included in the model. A: $x_{As} = 0.2, y_{As} = 0.2$; B: $x_{As} = 0.8, y_{As} = 0.8$; C: $x_{As} = 0.8, y_{As} = 0.8$; A: $x_{As} = 0.2, y_{As} = 0.8$. A notable shift in the levels can be observed [16].

2.4.4 Coulomb interaction

In the situation that more than one carrier is confined within the QD, Coulomb interaction, correlation (changes in the orbital shape due to Coulomb interaction) and exchange effects (Pauli exclusion principle) [2] arise [30], leading to the formation of distinct multiparticle states. The formation of these states may alter the absorption spectra and therefore the properties of the dot; any complete theory must take them into account. They can be calculated using the CI method [16], which consists of a basis expansion of the excitonic Hamiltonians into Slater determinants. Hence, Schrödinger equation for this states reads:

$$H^M|M\rangle = E^M|M\rangle \tag{2.22}$$

where E^M is the eigenenergy and $|M\rangle$ are the multiexcitonic states corresponding to N_e and N_h (number of electrons and holes respectively). The eigenstates of study are $M = X^0$,X^+,X^-,XX^0, i.e., the neutral exciton X^0 ($N_e = 1, N_h = 1$),the positive trion X^+ ($N_e = 1, N_h = 2$), the negative trion X^- ($N_e = 2, N_h = 1$) and the neutral biexciton XX^0 ($N_e = 2, N_h = 2$). These states are, at the same time, described in terms of the single-particle eigenfunctions Eq.(2.23). For example, for the neutral exciton X^0

$$|X^0\rangle = \sum_{i=1}^{N_e}\sum_{j=1}^{N_h}\eta_{ij}\begin{vmatrix}\psi_{ei}(\vec{r_e}) & \psi_{ei}(\vec{r_h})\\ \psi_{hj}(\vec{r_e}) & \psi_{hj}(\vec{r_h})\end{vmatrix} \tag{2.23}$$

In general, Eq.(2.23) and the equivalent for the other excitons are expressed as an expansion in Slater determinants functions, i.e.:

$$|M\rangle = \sum_m \eta_m|D_m^M\rangle \tag{2.24}$$

where m runs over electron and hole configurations, and the coefficients obey the normalization constraint $\sum_\nu |\eta_\nu|^2 = 1$. With this settled up, the system of equations to be solved variationally is:

$$\sum_\nu \langle D_n^M|H^M|D_m^M\rangle\eta_m = E^M\eta_n \tag{2.25}$$

The Hamiltonian can be decomposed in two components: $H^M = H_0^M + V^M$, H^0 the non-interacting term of the Hamiltonian and V^M introduces the Coulomb interaction. The matrix elements in the basis of Slater determinants are:

[2] A theory of how Pauli exclusion principle and correlation affect the absorption of photons by the QDs has not been proposed yet. They may alter the number of total absorbed photons and, therefore, the current. Further research in this topic should be done.

$$\langle D_n^M|H^M|D_m^M\rangle = \langle D_n^M|H_0^M|D_m^M\rangle + \langle D_n^M|V^M|D_m^M\rangle \tag{2.26}$$

The matrix elements of the Coulomb interaction are:

$$\begin{gathered}\langle D_n^M|V^M|D_m^M\rangle = \frac{1}{4\pi\epsilon_0}\sum_{ijkl}\int\int d\vec{r_1}d\vec{r_2}\frac{q_jq_i}{\epsilon(\vec{r_1},\vec{r_2})|\vec{r_1}-\vec{r_2}|}\cdot \\ [\phi_i^*(\vec{r_1})\phi_j^*(\vec{r_2})\phi_k(\vec{r_1})\phi_l(\vec{r_2}) - \phi_i^*(\vec{r_1})\phi_j^*(\vec{r_2})\phi_l(\vec{r_1})\phi_k(\vec{r_2})] = \sum_{ijkl}(V_{ij,kl} - V_{ij,lk})\end{gathered} \tag{2.27}$$

where $q_i, q_j \in [-e, +e]$. The first term on the integral would correspond to the direct Coulomb interaction whereas the second one to the exchange Coulomb interaction. V is defined as:

$$V_{ij,kl} = (1-\delta_{ij})(1-\delta_{kl})\int d\vec{r_1}d\vec{r_2}\psi_i^*(\vec{r_1}\phi_j^*(\vec{r_2})\left(\frac{q_iq_j}{4\pi\epsilon|\vec{r_1}-\vec{r_2}|}\right)\phi_k(\vec{r_1})\phi(\vec{r_2}) \tag{2.28}$$

Finally, the complete Hamiltonian components in the Slater determinant basis reads:

$$H_{nm}^M = \langle D_n^M|H^M|D_m^M\rangle = \begin{cases} \xi_n^{(e)} - \xi_n^{(h)} + \frac{1}{2}\sum_{i,j\in S_n}(V_{ij,ij} - Vij,ji), & \text{if n=m} \\ \frac{1}{2}\sum_{j\in S_n}V_{ij,kj} - V_{ij,jk}, & \text{n,m differ by one particle state} \\ \frac{1}{2}(V_{ij,kl} - V_{ij,lk}), & \text{n,m differ by two particle state} \end{cases} \tag{2.29}$$

where $\xi_n^{(e)}$ and $\xi_n^{(h)}$ is the sum of energies of the occupied single-particle (electrons and holes) states in the Slater determinant. The calculus of the six-fold integral Eq.(2.28) shows a demanding numerical procedure, which can be optimized using Green's function method. The numerical procedure will not be developed here, a further discussion on this topic may be found in [16].

2.4.5 Optical Properties

The optical properties of the QDs are the key part of their analysis, because they allow to define their suitability as photodetectors. The processes that may occur in the dot are intraband and interband transitions, which can lead to absorption and recombination. Intraband transitions happen within the same band (electron decay in the same band e.g.), whereas interband occurs between the valence and conduction bands. Decay probability is computed using Fermi's Golden rule; absorption and recombination are a sum of the different possible transitions. Putting it into math:

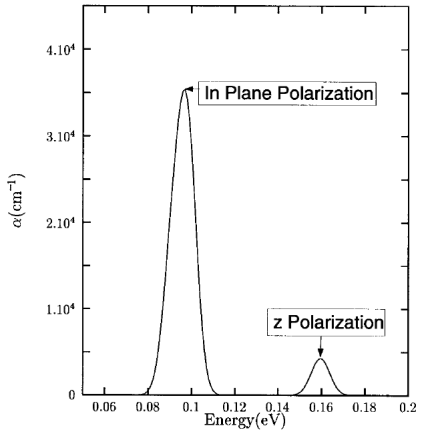

Figure 2.8: Absorption coefficient for a InAs/GaAs QD with base width 124$\mathring{A}$ and height 62$\mathring{A}$.The plane polarization is absorbed much more efficiently than the z-polarization [12].

$$\widehat{P} = \sum_{n,m} \langle \psi_f^n | \nabla | \psi_i^m \rangle, \tag{2.30}$$

$$\langle \psi_f^n | \nabla | \psi_i^m \rangle = \sum_{j,k}^{8} \langle F_j u_j^\Gamma | \nabla | F_k u_k^\Gamma \rangle = \sum_{j,k}^{8} \left[\delta_{j,k} \langle F_j | \nabla | F_k \rangle + \langle F_j | F_k \rangle \langle u_j^\Gamma | \nabla | u_k^\Gamma \rangle \right] \tag{2.31}$$

The radiative or recombination rate is defined:

$$R \equiv \Gamma_{fi} = \left(\frac{e}{m} \right)^2 \frac{2\hbar\omega}{c^3} |\langle f | e \cdot \widehat{P} | i \rangle|^2 \tag{2.32}$$

Here, $\hbar\omega$ stands for the radiation energy, $|i\rangle, |f\rangle$ for the multi-particle states (Eq.(2.24)), $|\psi_i\rangle, |\psi_f\rangle$ for the single-particle states. In addition, F_j is the envelope function, and $\vec{e}$ the polarisation vector. The absorption coefficient can be estimated as follows:

$$\alpha(\hbar\omega) = \frac{\pi e^2 \hbar}{\epsilon_0 n_0 c m_0^2 V} \sum_f \frac{1}{\hbar\omega} |\vec{e} \cdot \widehat{P}|^2 \frac{1}{\sqrt{2\pi\sigma}} exp\left((E - \hbar\omega)/2\sigma^2 \right) \tag{2.33}$$

This coefficient will be key in the design of photodetectors and is, for QD, extremely peaked (see Fig. 2.8 and Section 2.5); basically, it describes how well radiation can be absorbed depending on the energy. This absorption spectra is tunable by adjusting the size of the dots, what makes them interesting for photodetection as well as emitting almost monochromatic light. This topic will be covered in more detail later on, in Chapter 3.

The gain of the material is given by:

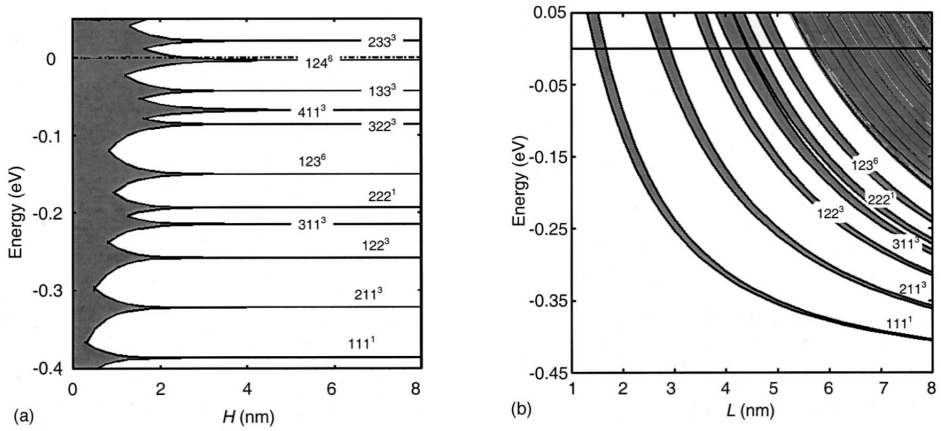

Figure 2.9: a) Mini-band as a function of the interdot distance. b) Mini-band as a function of size (for H=15nm) [21].

$$g(\hbar\omega) = \frac{\pi e^2 \hbar}{ncm^2 V} \sum_{ij} |\vec{e} \cdot \widehat{P}|^2 \frac{1}{\pi} \cdot \frac{\hbar/\tau}{(E_i^e - E_j^h - \hbar\omega)^2 + (\hbar/\tau)^2} (f^e(E_i^e) - f^h(E_j^h))^2 \tag{2.34}$$

The gain is important to estimate the Quantum Efficiency (both internal and external) of any photodetector. It is related with the number of charge carrier pairs created as a function of the incident radiation, i.e., number and energy of incident photons.

2.4.6 Mini-band formation

So far interactions and energy levels within the QD have been covered, however considerations about how QDs interact among them have not been taken into account. When they are placed close to each other, a significant wavefunction overlap arise and the discrete energy levels split into mini bands. For this case, discrete does not refer to the energy levels of the own QD, but to the non-interference of them. In Fig. 2.9, the energy levels are plotted against the distance between QDs of an array (a) and against the size of the QD (b):

As interdot distance increases and wavefunction overlap decreases, mini-bands reduce to discrete levels, which is clear in Fig. 2.9 *a*). In Fig. 2.9 *b*) mini-bands show a discrete behaviour which turns to continuum above the barrier potential.

In following sections, and taking as reference the results obtained in [21], QDs arrays will be thought to be composed of single QDs that do not interact among them. This is to very short distance a good approach, simplifying the calculi required.

2.5 Simulations

The aim of this section is to prove the concepts presented above about QD's electronic structure. The software used has been *Quantum Dot Lab* developed by *nanoHub.org* [24], a non-profit organization funded by the *United States National Science Foundation*. It is focused on professional networking and interactive simulation tools for nanotechnology. The software allows to adjust the size (in the three spatial dimensions) of the dots, as well as the lattice constant, effective mass, bandgap energy and total number of states (8, following the 8kp method). The theoretical analysis provided in Section 2.4 is included in the simulation. Other features can also be adjusted, such as the angle of the incoming light [3], the temperature (room temperature is assumed) and electron Fermi level.

The material chosen for the simulations is germanium, since it is proposed in this work for photodetection, as was presented in Section 2.2.1. Simulations of Si-QDs have not been done due to their more limited wavelength spectra [5] (see Subsection 3.2.2 for more information).

The input data in both cases are: a bandgap $E_g = 0.67$eV, electron effective mass of $m_e^* = 0.041m_0$ and lattice constant of $a = 5.65$Å, all in a dome shape. The radii of the QDs are $r = 4.5$nm in the first simulation and $r = 8.5$nm in the second.

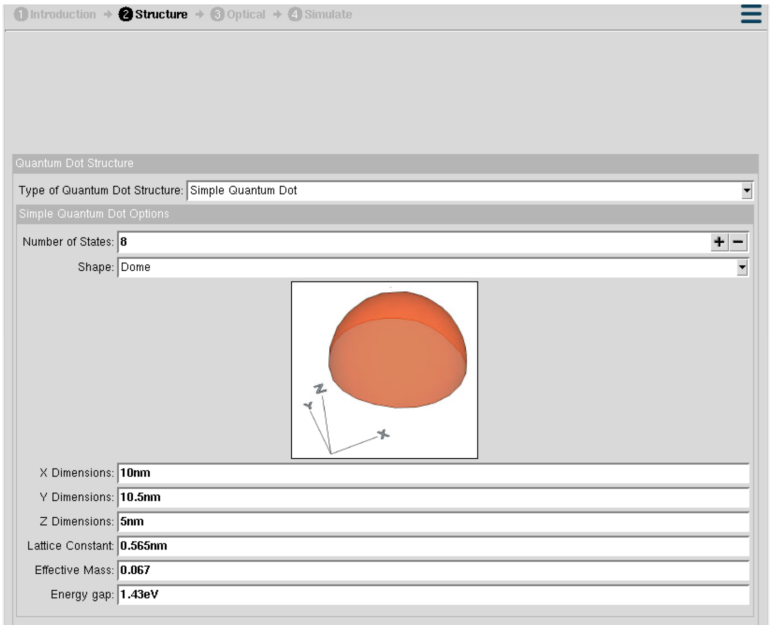

Figure 2.10: Quantum Dot Lab interface.

[3] Light was considered linearly polarized in all the simulations carried out

First Simulation (I)

The simulation yields a bandgap energy of 2.114eV, much higher than the original 0.667eV; this proves how the electronic structure of the semiconductor is affected by the strain energy necessary to form the QD. The diagram shows the first and second excited states, proving the atom-like behaviour of nano-scaled QDs.

The absorption profile has also been calculated: two sharp peaks, corresponding to the first and the second excited state are observed. They occur at the energies of 2.114 eV (586.2 nm) and 2.476 eV (500.3 nm) respectively. The absorption under radiation is quantized in discrete values, each one corresponding to a peak (an excited state). According to Fig. 2.11 and Fig. 2.12, this QD configuration will be suitable for photodetection within the visible spectrum (green colour, to be precise).

In Fig. 2.12, a comparison between the absorption peaks at different polarization angles is given: For $\theta = 0°$, the absorption peak occurs at the first excited level, whereas for $\theta = 90°$ it occurs at the second one. Polarization angle ϕ was kept at 0° in both cases. This effect must be addressed and corrected in the design of any photodetector, for example using lenses that filter the light to the desired polarization. For instance, for a perpendicularly polarized ray ($\theta = 0°$), there will be an unique sharp peak of absorption, so in principle no colour filter would be necessary (see Subsection 3.1.1).

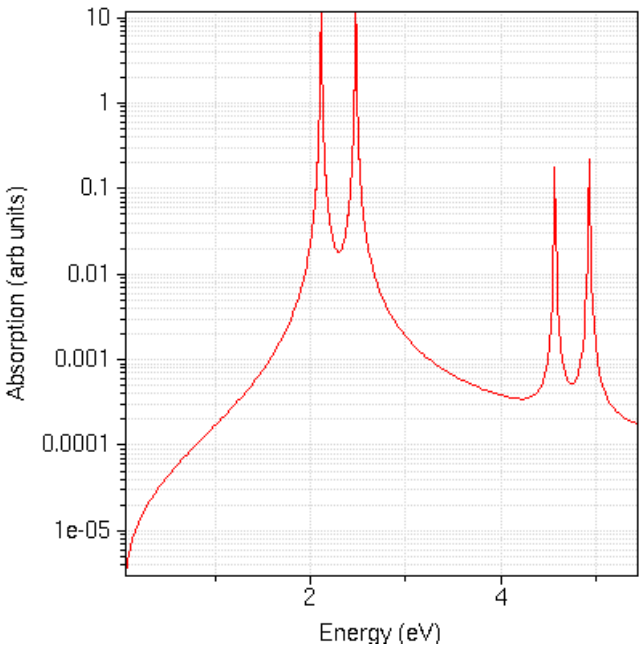

Figure 2.11: Absorption spectrum of the Ge QDs (I).

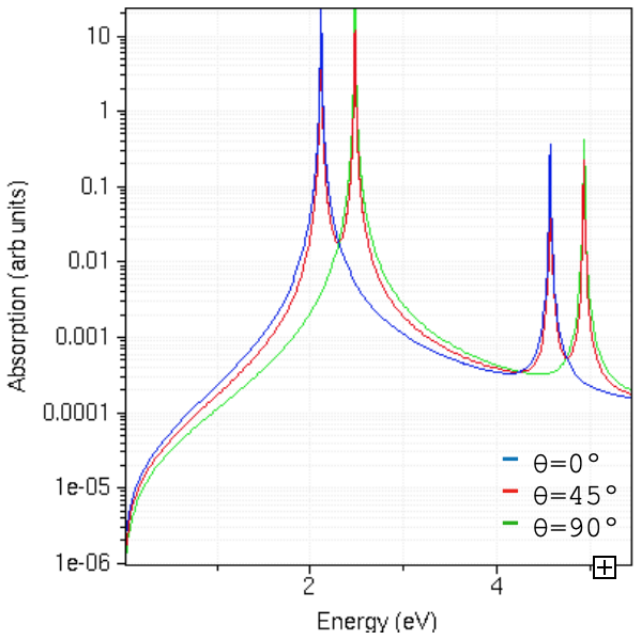

Figure 2.12: Comparison of the absorption spectra for different polarization angles (I).

Second Simulation

In this case, the band gap energy decreases to 0.5673 eV (around 0.10 eV less than the bulk Ge) and the second excited state is placed 0.6514 eV above the ground state. Although the radius difference is only 4 nm larger than in the first case, the differences are significant. Therefore, an extremely precise control on QDs is required to allow absorption of light in the desired wavelength.

The absorption peaks are completely shifted from the ones of the first simulation: the first one happens at 0.5673 eV (2.184μm) and the second at 0.6514 eV (1.902μm). Photodetection still remains possible, but this time within the SWIR range. Again, a sweep from polarization angle θ from 0° to 0° yields to absorption peaks at the angle boundaries; polarization angle should also be corrected with a filter.

These simulations have been useful to prove the atom-like behaviour of QDs, as well as their tunability depending on the size. However, precise simulations should be carried out using more complex simulations, considering not only the QDs, but also the layers that surround them and have an influence in absorption too. Without that all-in-one simulation, a description of the optoelectronic characteristics of a QDPD is incomplete. It is, however, beyond the scope of the present thesis. Experimental results reported from proof-of-concept devices will be provided in Chapter 3 instead.

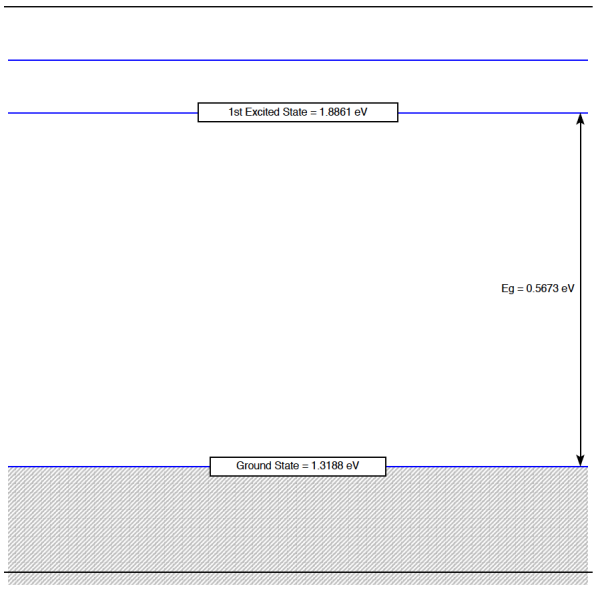

Figure 2.13: Energy states (II).

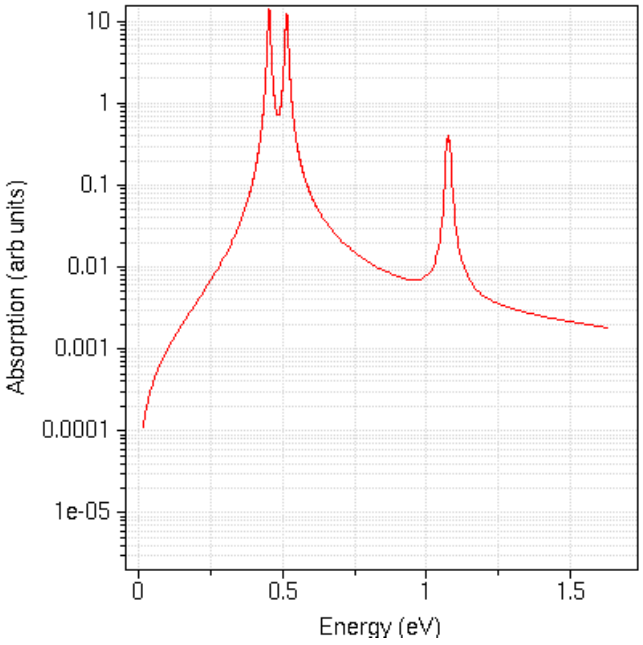

Figure 2.14: Absorption spectrum of the Ge QDs (II).

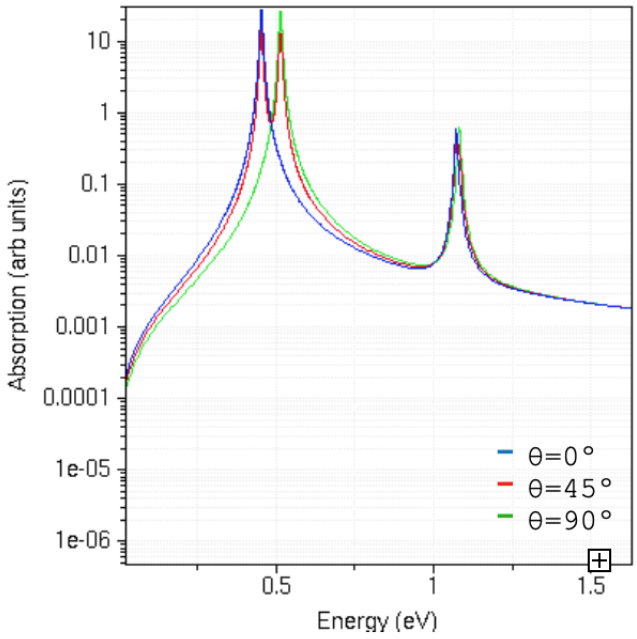

Figure 2.15: Comparison of the absorption spectra for different polarization angles (II).

Chapter 3

Photodetectors

3.1 State of the Art

3.1.1 Visible Spectrum

Colour sensing is the main goal of photodetectors, allowing to capture images within the visible spectrum. This technology has experienced an outstanding improvement in the last two decades, with the massive expansion of digital photography. Before introducing the new sensing technologies based on QDs, a short discussion on the current state of art of photodetectors is in order.

Colour sensing must cover wavelengths between 400 and 700nm approximately [18],[17], absorbing the incident radiation and transforming it in an electrical signal. Apart from imaging, colour photodetection is widely used in spectroscopy, fluorescent biomedical imaging, industrial inspection, etc. [26][22][28][40]. Silicon devices are of common use in this part of the spectrum, due to their good optical properties, abundance and developed manufacturing techniques. Although there are many kinds of silicon photodetectors, the two main types are photodiodes and photogates. Both are based on the photoelectric effect, first explained by Einstein [9]. Basically, they convert the incident photon flux of light in electron-hole pairs. If a photon has sufficient energy it will excite an electron from the valence band and promote it to the conduction band, where electrons can move freely. This sufficient energy is the band gap energy ($E_g = 1.124$ eV for Silicon [34]) and, when applied, creates an electron-hole pair.

Under certain bias conditions, some of the pairs are converted into photocurrent. This

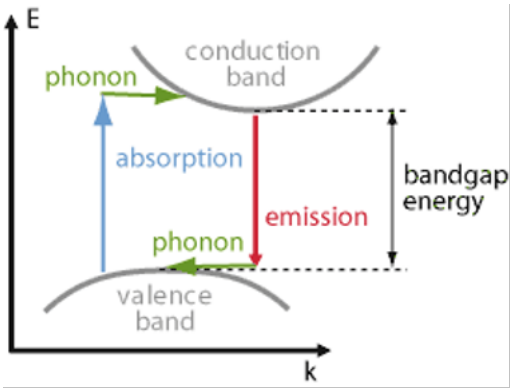

Figure 3.1: Simplified diagram showing the absorption and emission processes in a semiconductor [27].

current is in the order of nA, pA, so it has to be integrated with the help of a capacitor; in this process the main difference between CCDs and CMOSs arises. More information of CCDS and CMOSs sensors can be found in Appendix B.

Photodiode

It is composed by an implanted n-region buried in a p- substrate, creating a depletion area between them. This zone is depleted of carriers and has a certain electric field; this electric field pushes the electrons to the n region, and holes to the p region, generating a photocurrent. Photodiodes are usually operated in reverse bias, with a positive voltage between n and p region. The generated current is then transferred to the read-out circuit and interpreted. Focusing on the performance, photodiodes are limited to a 100% quantum efficiency (one charge carrier per photon, at most). Transient times (also called temporal photoresponse) are within the range of the nanoseconds, enough to fulfill the requirements of imaging. Any new technology aiming to replace Si-based photodiodes should exhibit figures of merit of this order [18].

Photogate

The photogate consists in a silicon gate buried in an insulator (typically SiO_2), with a depletion region below. Due to the electric field in the depletion region, charge carriers are separated and either electrons or holes are collected by the photogate. For instance, for a p- substrate with a n channel region near the surface (Fig. 3.3), the photogate collects electrons. The electrons and holes pairs are created in the depletion region; electrons are

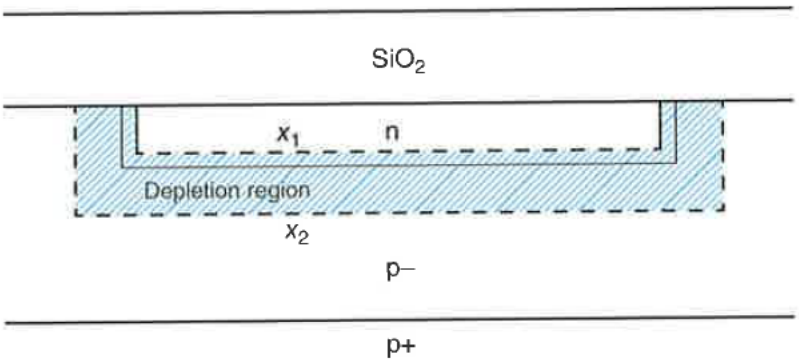

Figure 3.2: Diagram of an standard silicon photodiode [18].

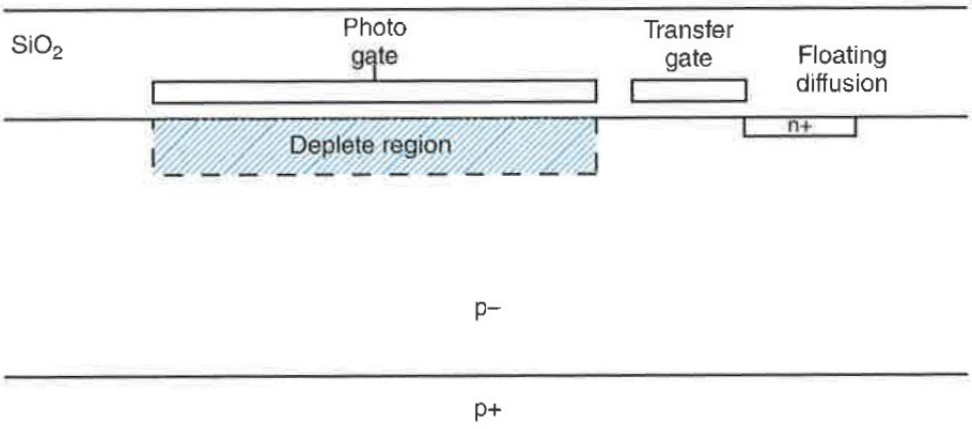

Figure 3.3: Cross section of a photogate [18].

held in the potential well, while holes are collected in the substrate.

Typically, photogates are less efficient because of the photon absorption in the gate. This effect can be counteracted using other materials for the gates such as Indium Tin Oxide (ITO), which will also be used to improve QDPD efficiency [18] [23].

Pixel Optics

Each of the sensing parts in a sensor are called pixels: they are the minimum detecting unit of digital image. Within a pixel, different parts can be identified: the microlens, filter, passivation, metal and the substrate.

The microlens focuses the incident light on the detector, to optimise the absorption of incoming photons. The colour filter is used to spectrally separate incoming photons, allowing pixels to have different responsivities. In a RGB system, called Bayer Pattern,

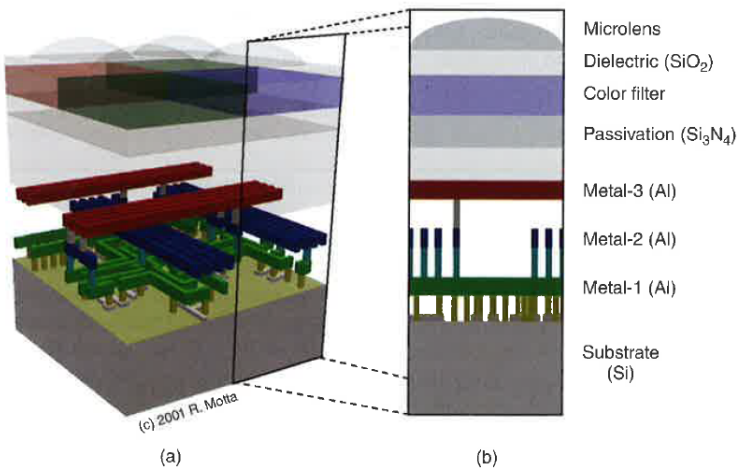

Figure 3.4: CMOS image sensor, layer by layer [18].

every pixel detects a certain colour and then the software reconstructs the full colour image with the information of each of the pixels. A more sophisticated colour pattern is the quad pixel sensor [4].

Photodiodes are found under the colour filter, followed by a metal structure whose main task is to transport the charges. On the bottom is the base of the pixel, the Si substrate, which is responsible for photon absorption.

3.1.2 Infrared spectrum

Infrared detectors, though less used than sensors in the visible spectrum, are experiencing an outstanding increase in the number of possible applications. Besides night surveillance (their first application, for military and civil purposes), they are being used for optical tomography, process monitoring, Lidar sensors, advanced driver's assistance (obstacles detection), augmented reality, biometrics, etc. [23][28]. Many of these applications require high fidelity and a massive production of these IR detectors at a low cost. Silicon-based products, though cheap and highly optimised, are not suitable for these tasks, because of the Si absorption decreases around wavelengths of 900 nm [22].

A short discussion about infrared radiation is in order, to understand the range of possible applications for QDPDs. Infrared covers the range from approximately 0.75 μm to 12 μm; within this range, different regions can be distinguished: Near-Infrared (NIR),

[4]Difference among them in https://news.skhynix.com/evolution-of-pixel-technology-in-cmos-image-sensor/

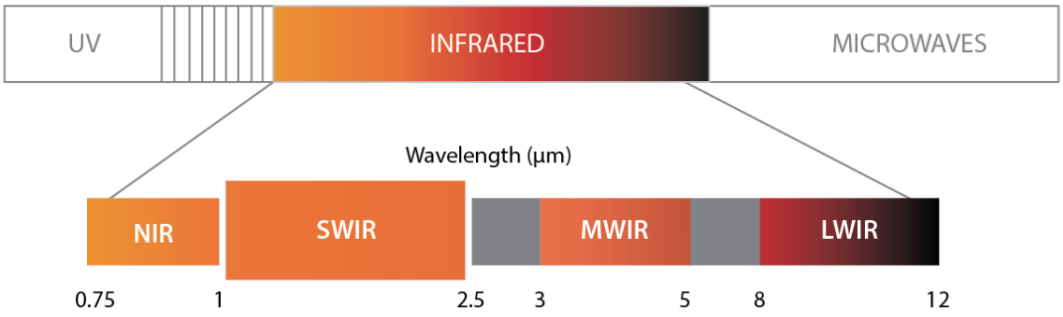

Figure 3.5: Current IR spectrum and its imaging standard ranges [36].

Short Wave Infrared (SWIR), Medium Wave Infrared (MWIR) and Long Wave Infrared (LWIR) [36].

In this work only NIR and SWIR will be considered; performance of QDs in MWIR and LWIR detectors is still very poor and requires equipment cooling [22]. Besides, few QDPDs have been reported in this range, so the technology still needs much more development to consider it an alternative to common MWIR-LWIR detectors.

Characterization of Photodetectors

Current imagers in NIR use silicon circuitry for pixel read-out in combination with flip-chip (an assembling technology) bonded III-V materials, such as InGaAs, HgCdTe or InSb [22][17]. They have a substantial higher cost than average image sensors based on CMOS technology in the visible spectrum, since they have to be grown by high-temperature epitaxy on small wafers sizes, mostly using MBE. For example, SWIR imaging is mainly achieved with $In_{0.53}Ga_{0.43}As$ with a substrate of InP; they exhibit a 0.73 eV bandgap. However, they are not completely integrated in the silicon, what increases their cost. A disruption in the manufacturing process is not expected in such a mature technology [22]. These limitations reduce the implementation of IR cameras to specific fields, setting them apart from a widespread use.

IR radiation, defined by its wavelength lambda and optical area A_0, impinges on an optical concentrator (a lens), which focuses the beam towards the electric area Ae of the absorber material. This absorber is stacked between metal contacts and a substrate (typically a silicon-based material), as shown in Fig. 3.6.

For the absorber, InGaAs can be tuned from a bandgap of 0.35 eV (InAs) to 1.43 eV

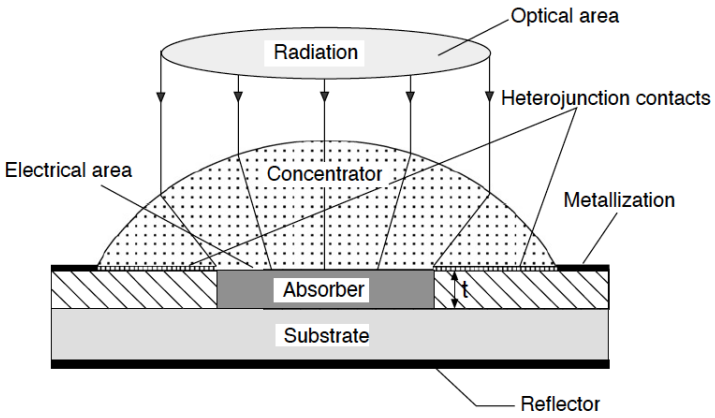

Figure 3.6: Cross section of a typical IR sensor [28].

(GaAs), that is, from wavelengths starting at 0.87 μm to 3.5 μm, a quite broad tunable bandgap, that covers most of the infrared spectrum. They show the best performance in NIR, because of their high detectivity, high QE, low thermal noise and ability to function at room temperature [4]. However, they have a limited response range due to optical absorption in the window layer or substrate, what narrows the absorption spectrum. New hybrid systems are being launched to overcome this limitation, like the InGaAs-graphene phototransistor, proposed by [4]. However, devices based on graphene are still not applicable to mass production.

HgCdTe has the broadest spectral range (1μm to 25μm.), together with a high absorption coefficient and a high quantum efficiency, while keeping low thermal generation. However, there are a few problems with this alloy: mass production is very complex, as a consequence of weak Hg-Te bond, the phase diagram is not stable and therefore standard uniform composition bulk crystal are difficult to obtain. Besides, their toxic compounds can cause health hazard. All these limitations restrict the use of $HgCdTe$ alloy to special devices, mostly for LWIR purposes, while $InGaAs$ is used in NIR and SWIR and $InSb$ in MWIR.

Despite of the advanced current progress in IR technologies, all the issues presented here are a strong motivation to develop new cheaper, adapted to silicon growth techniques and reliable imaging technology. This work will focus on how quantum dots can fulfil all these conditions, with an emphasis on adapting them to the current manufacture standards. In other words, it is not the aim of this work to discuss breakthrough technologies, but to present small steps that can be assumed on the short term.

3.2 QD Photodetectors

Quantum Dot photodetectors are a promising new technology to overcome existing IR sensors and even VIS-Si sensors. They have important advantages, such as: spectral sensitivity control of the detectors by QD size, detection under normal incidence of light, lower price (in IR sensing, mostly), processing on a large area, smaller pixel pitch, etc [8],[40]. Active research has been carried out in the last decade, what has brought QDPD to technological readiness level 3 [22], although the SWIR camera reported by *SWIR Vision Systems* [36] proves that the posible next stage has been achieved. This method for judging the maturity of technologies was first proposed by the NASA [38] and has become an standard within the UE too. Level 3 means that an active level of research has been reached and a proof-of-concept has been constructed. The main targets to bring QDPD to an industrial level can be summarized in three points: material, device and camera integration challenges.

Material challenges include finding the right component for the dot, considering how its properties vary from the bulk material to the final dot and adjusting them to the spectrum to be detected. In following sections, behaviour on this topic for lead sulphide (PbS) and germanium (Ge) will be further explained. The other aspect that should not be forgotten is material's cost for scale-up production, availability in different parts of the world and non-dependence on a single supplier [26]. In the case of PbS, the estimated cost of active material per photodetector is around 0.15 US Dollar (0.13€) and similarly with Germanium QDs. For a production of 10 million devices, 50kg of material would be required, what can be easily covered by annual production [22]. Thus, materials are not a limiting factor.

Device challenges include knowing accurately the electronic structure of the QDs and transitions involved in photon absorption. These are well known for bulk semiconductors, but not with the same level of detail in QDs. One of the latest models published has been introduced in Chapter 2, but light-matter coupling, low current, good responsivities, etc must be further investigated.

Camera integration is the last step to be solved before mass production. Quantum Dot photodetectors must be compatible to the current industrial fabrication flow based on Silicon, to allow process optimization and consequently low prices. Besides, standard camera sizes should be achieved. In following sections these steps will be addressed, giving

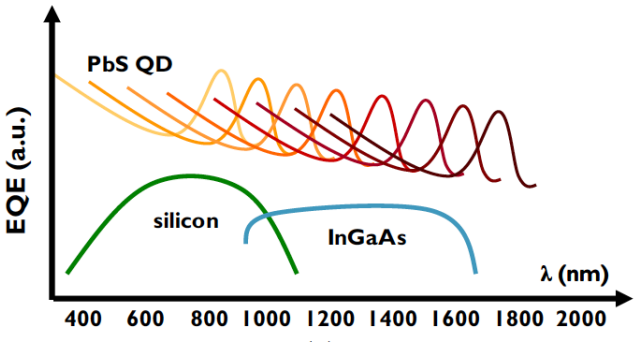

Figure 3.7: Schematic comparison of EQE between silicon, InGaAs and PbS QDs [23].

a complete picture of the advances carried out in this research field.

3.2.1 PbS Quantum Dot Photodetectors

Colloidal Quantum Dots have reached an established status as light sources in displays [29], what has increased the interest in other applications such as infrared detection. Great progress has been achieved in QDs sensing technology in the recent years, enough to consider them a viable option for mass market applications.

PbS QDs enable the detection in the NIR, SWIR, due to their tunable optical properties depending on the size. By varying the dot size from 2 nm to 10 nm, the whole SWIR spectrum can be covered (700-1800 nm) [17]. In Fig. 3.7, a comparison of the absorption spectra between standard silicon (for the visible spectrum) and InGaAs (for the IR) is plotted. Taking advantage of the large exciton Bohr radius, PbS QDs cover most of the range of wavelengths of interest, while showing a better external quantum efficiency.

QD size has a strong influence in the optical properties, as it has been shown in Section 2.5, being the absorption peak linearly dependent with the size, according to [23]. For example, a QD with diameter 5.5nm has an absorption peak around 1440nm, while dots as big as 10nm diameter have been reported [8] (for photodetection). With such small dots, the pixel pitch limit is set by the CMOS ROIC, unlike in InGaAs sensors.

Fabrication Process

PbS photodiodes are designed with an n-p junction architecture. The fabrication process starts by cleaning the substrates (Si/SiO_2) with a standard detergent. Then, a metal oxide electron transport layer (ETL) is deposited on the substrate, acting as the bottom

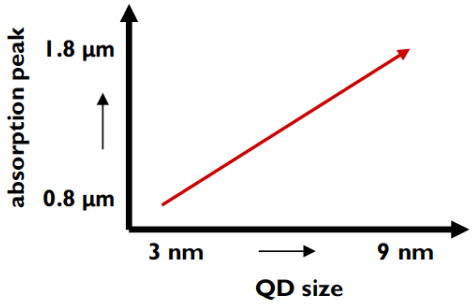

Figure 3.8: Absorption peak depending on dot size [23].

contact, to improve electron transport. TiO_x, ZnO or TiN are used for this layer, thanks to their high reflectivity in the IR range and compatibility with the CMOS process. This layer is annealed at high temperature, which makes it interesting for deposition before the QD layer (to avoid melting). Another approach for this layer under development is the use of Transition Metal Dichalcogenide (TMDC) for high-mobility transport layers [35]. They can provide good IR absorption as well as a good transfer of charges to the contacts for charge collection. MoS_2 and WS_2 have been proposed for this layer.

Afterwards the QD film is deposited layer by layer: the colloidal QD solution is deposited by spin-coating in the ETL layer ($15 - 50$ nm each time) and repeated until the desired height is obtained. The thickness is a trade-off: the thicker it is, the more photons that are collected, but the more difficult to assemble. As explained in Section 2.3.1, QDs may also be printed according to recent studies [35]. On top of the stack a hole transport layer is deposited, a p-type polymer, designed to transport the holes. For example, in [35] the material chosen was Spiro, named after ,2',7,7'-Tetrakis[N,N-di(4-methoxyphenyl)amino]-9,9'-spirobifluorene, a perovskite commonly used for hole transport layers (HTL). The QD structure is finished with a semi-transparent top contact that allows top-side illumination, usually made of evaporated silver (Ag) or sputtered ITO. An optimised version of an ITO top contact is able to significantly improve the light harvesting and thus EQE, while preventing electron's back injection. A convenient solution for this layer manufacture is presented in [26]: gold source and drain contacts are patterned on the TMDCs using photolithography; this might speed up production.

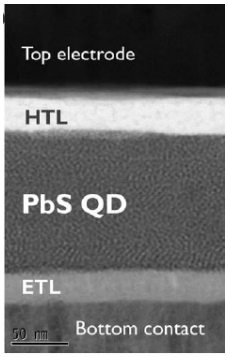

Figure 3.9: Cross image of the QD stack, obtained using annular bright field scanning transmission electron microscopy [8].

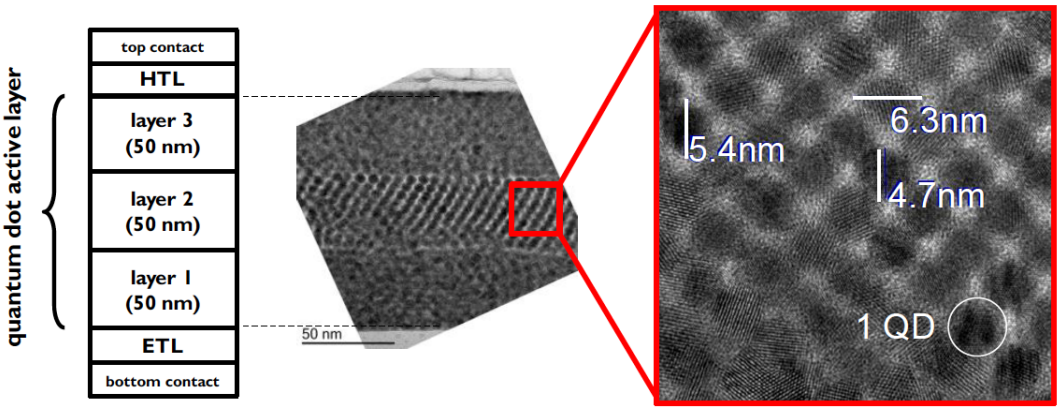

Figure 3.10: Cross view of the stack, schematic (left) and obtained by transmission electron microscopy [23].

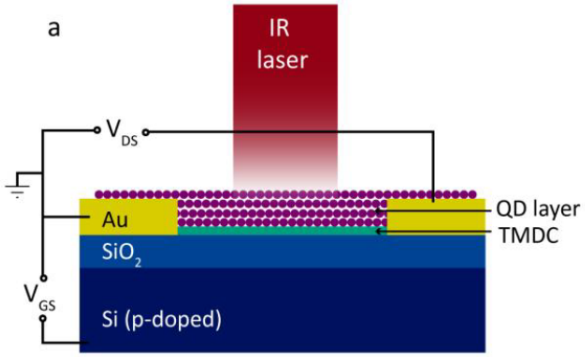

Figure 3.11: Photodetector with circuit diagram, includind the TMDC layer [26].

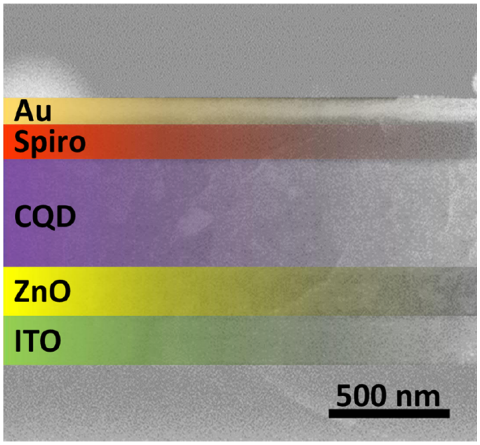

Figure 3.12: Scanning electron microscopy representing the full QD stack [35].

QD Performance

A proper evaluation of the QD photodetector properties is necessary to judge whether they can be a feasible alternative for IR sensing. The main figures of reference will be analysed here and compared with well-established technologies presented before.

The first value to consider is the dark current I_d, measured at room temperature. In [8], a value of 29 nA/cm^2 at an applied reverse bias of -1V is reported, showing a photocurrent-to-dark current ratio of 90dB. Meanwhile, in [23] 6 μA/cm^2 at reverse bias -2V. The reference value for an InGaAs detector is below 20 fA/cm^2: PbS QDs cannot beat this target value, although presents a sufficiently low value for imaging purposes. It is of interest to remark how dark current can be drastically reduced by cooling the equipment: at 193K, dark current ratio was improved from 30dB at room temperature to 62dB [23]. However, the aim of this work is to provide solutions for standard utilization at room temperatures, without cooling. In both cases a linear scaling of dark current with pixel size is observed, an important result to achieve high resolution devices.

The EQE achieved is of 21% on top illuminated devices for $\lambda = 940$ nm [8], raising to 25% with optimized semi-transparent contacts [23] at $\lambda = 1440$ nm. A detailed graphic of the EQE as a function of the wavelength is provided in Fig. 3.13; it can be seen that the higher efficiency is achieved within the VIS spectrum, with peaks of 90% (for the QD configuration chosen), and drastically decreases over $\lambda = 1000$ nm. These values are lower than InGaAs based photodetectors, but still higher than Si PD. The detectivity $D*$ rises to 10^{12} cmHz$^{1/2}$W^{-1} in both [35][8], same as for TMDCs hybrid PD, with 10^{12} Jones

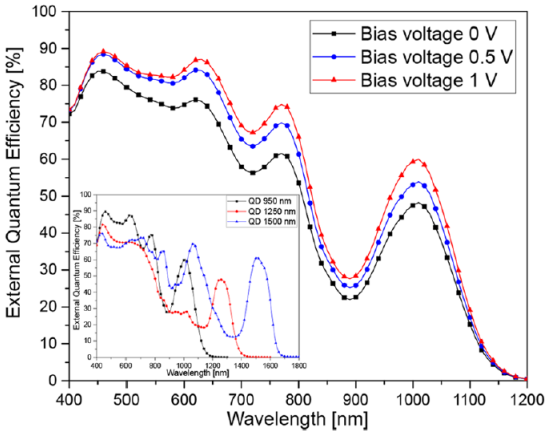

Figure 3.13: EQE comparison for different bias voltages and wavelengths [35].

[5] (WS_2) and $2.8 \cdot 10^{12}$ Jones (MbS_2) [26], whereas an average InGaAs detector shows a detectivity of $6 \cdot 10^{12}$ Jones.

Another figure of merit is the photo-response, which shows how fast photocurrent is conducted. First, the rise time from 10% to 90% of the photogenerated signal is measured (τ_{rise}) and then the fall time (90% to 10%). Rise and fall times of 57 μs and 86 μs were obtained under perpendicular illumination in [8], further improving this value in [23] to 13 μs and 41 μs. This performance is sufficient for basic imaging applications, but shorter times should be achieved for more demanding imaging applications (high speed cameras, video, etc). Limiting factors, like trap states or interface defects, should be further investigated, to approximate them to values registered in InGaAs PD ($\tau_{rise} = 0.65$ μs, $\tau_{fall} = 2.20$ μs [4]. For TMDC hybrid devices, $\tau_{rise} = 0.032$ μs(WS_2) and $\tau_{fall} = 0.20$ μs (MbS_2), under illumination $\lambda = 1310$ nm. Ink-printed QD yield values of $\tau_{rise} = 4.4$ μs and $\tau_{fall} = 8.2$ μs [35] [26]. In these devices, response is far from the benchmark values of current technologies. This might be caused by trapped electrons in the QD, that limit the charges flow to the transport layers.

Integration Aspects

QD photodetectors under investigation and testing phase are mostly manufactured using slow techniques, such as manual scrubbing for the cleaning of the contact pads. Any currently standardised process for the mass market is based in photolithography, a highly accurate fabrication process flow [10]. The next step to incorporate QDPD to cameras is

[5] 1 Jone is equal to 1 cm $\cdot$ $\mathrm{Hz}^{1/2}\mathrm{W}^{-1}$

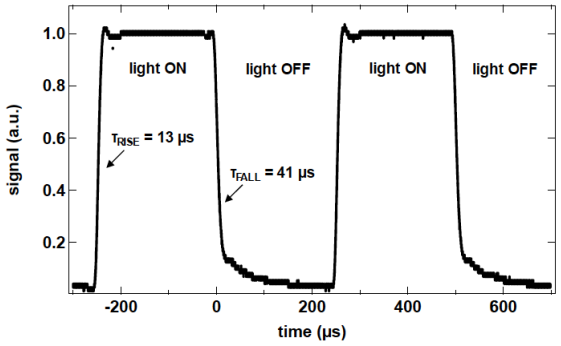

Figure 3.14: Transient photoresponse [23].

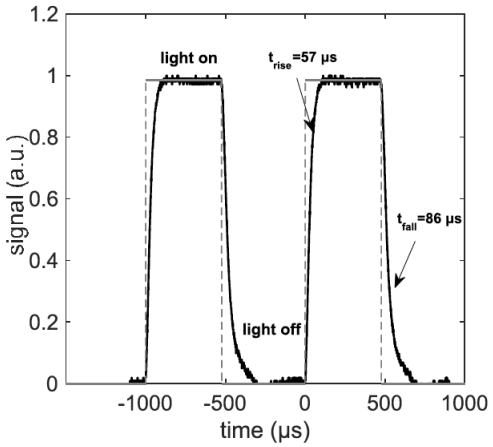

Figure 3.15: Transient photoresponse [8].

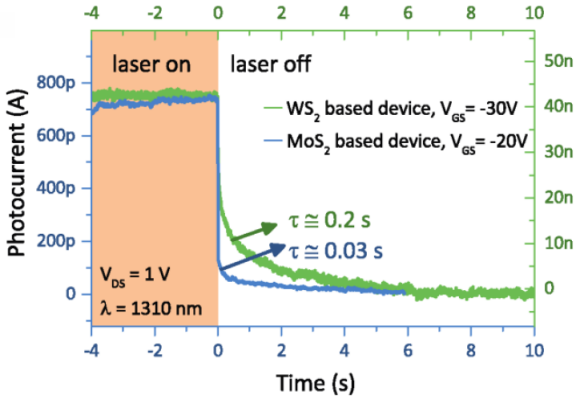

Figure 3.16: Relaxation times [26].

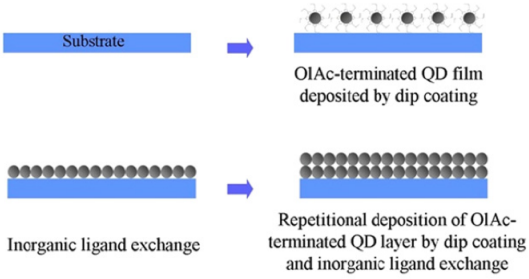

Figure 3.17: Deposition of QD layer [10].

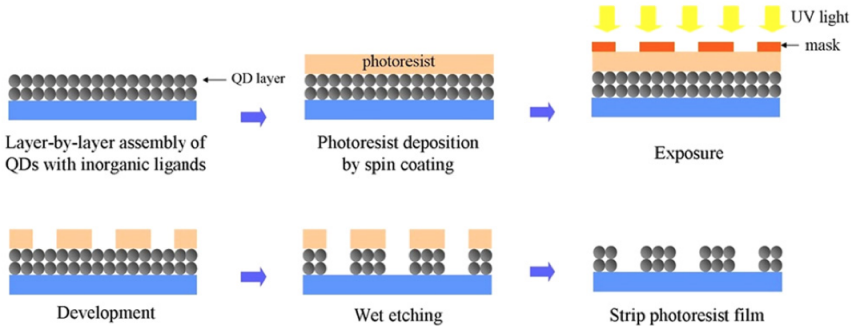

Figure 3.18: QDs islands obtained with photolithography techniques [10].

to adapt them to a silicon-based ROIC and pattern the dots and contacts on it.

A photolithography technique for lead chalcogenide (PbS) QDs has been proposed in [10]. First, QDPD is patterned to create an island that covers the entire focal area. A stack solution of S and $PbCl_2$ is deposited by dip-coating, together with a ligand (OlAm), all at a temperature of 160°C. After that, OlAm ligands are substituted by oleic acid (OlAc), to obtain a ligand shell that stands consecutive cycles (Fig. 3.17).

The following process flow of QD patterning is shown in Fig. 3.18. Starting with the previously obtained QD layer, a photoresist layer is applied and "baked" to fix it to the lower layer. Afterwards, a pattern is transferred using a photomask and UV radiation. Then, an HCL/H3PO4 mixture is prepared as etchant to remove the uncovered parts of the QD film. At last, acetone is applied to the photoresist to remove it, obtaining the desired QDs islands. A similar process was followed in [8], but including the electron and hole transport layers, as well as the contact pads. The only remaining step is packaging the detector, a non-problematic process (average Si detectors packaging may be used).

With this method, the pixel pitch is exclusively defined by the ROIC, so sizes in the order of state of the art Si imagers are possible. Pixel arrays with pixel pitch of 40 μm have been obtained, with successful pixel isolation (no cross effects between pixels). However,

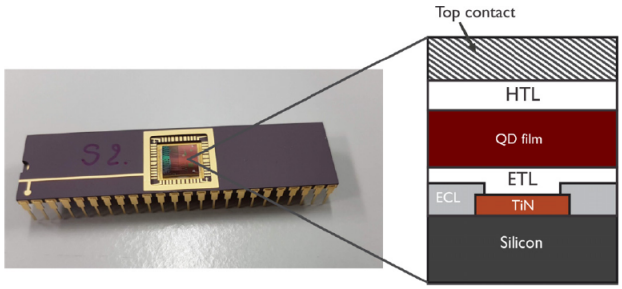

Figure 3.19: Packaging of the sensor (left) and cross-section scheme of the photodetector (right) [8].

this pixel pitch is still big compared to average CMOS image sensors.

Multispectral Photodetectors

It would be desirable that multispectral sensors cover both visible and NIR wavelengths, enabling normal cameras to enhance their performance in low light conditions, or offering industries process a more detailed inspection, among other possible uses. The tunability of QDs allows to design devices that can accomplish this wide-spectrum detection.

Two approaches are possible: detector with both IR and VIS specialized photodiodes (Fig. 3.21) and photodetectors that show dual-spectrum detection (Fig. 3.20). The first one, proposed in [8], is a hybrid system between PbS QDPD and common Si photodetectors, all assembled in the same ROIC. The second one is a more complex structure: Two stacked PbS QDPDs are placed one on top of the other, each one with QDs of different size. Thus, each layer is specialized in a region of the spectrum; the top detector is made of small QDs that detect the visible spectrum, while the buried one is made of larger QDs that detect light in NIR and SWIR. The top layer also acts as a filter for visible light, since larger PbS QDs may also absorb radiation in the visible; with this configuration, the spurious sensitivity to visible in the buried detector is almost suppressed.

A hybrid system of colloidal QDs and Si pixel has not been tested yet and remains as a concept. Meanwhile, the double QDPD has been proved [8], yielding responsivities as high as 300 A/W. However, a detailed study of these devices still lacks in order to compare its behaviour with both VIS and IR reference photodetectors. It remains a future research topic.

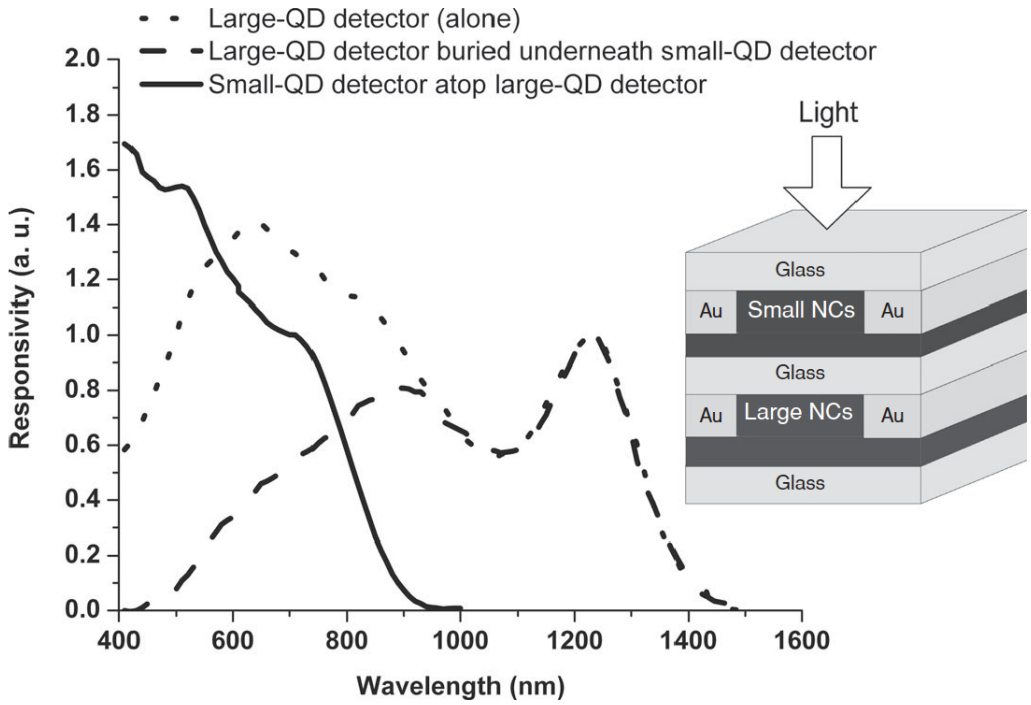

Figure 3.20: Responsivity comparison of three configurations of QD detectors (left) and diagram of the dual stack multispectral QDPD (right) [17].

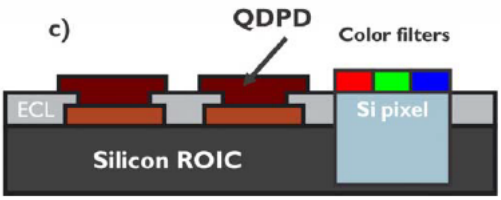

Figure 3.21: Schematic figure of a hybrid multispectral sensor, composed by a Si pixel and a QDPD [8].

3.2.2 Ge Quantum Dot Photodetectors

Group IV quantum dots have attracted much interest due to their compatibility with Si technology and very large-scale integration possibilities. Like PbS QDs, they can offer tunability from UV to IR, while showing a high quantum efficiency. Although Silicon QDs are easier and cheaper to manufacture, they have a more limited wavelength spectra. Germanium QDs, while still highly compatible with Si substrates and fabrication processes, offer a wider spectrum, lower synthesis temperature and larger excitonic Bohr radius (stronger quantum confinement) [5][32]. Besides, it has higher carrier mobility than Si, is non-toxic, electro-chemically stable in time and relatively cheap compared to other options (such as InGaAS).

Highly accurate manufacture of these devices is a key factor to guarantee uniformity of the optoelectronic features. Defects, mid-gap states or the degree of crystallization may affect the performance of Ge-based devices.

Fabrication process

Different fabrication processes have been reported, using different deposition techniques. In [19], QDs were grown by ultrahigh-vacuum chemical deposition on a Si buffer layer of 50 nm. After deposition, self-assembled dots were formed at 600°C under Stranski-Krastanov mode. Another fabrication process consists in using rf-magnetron sputtering [6] deposition of SiO_2 and Ge on a n-Si substrate, maintained at 400°C [5] [32]. The deposited film is then annealed at 500°C in a N_2 atmosphere, in order to generate densely packed Ge QDs. Thicknesses as low as 25 nm can be achieved, although they can also exceed hundreds of nanometers.

Regarding the compatibility of Ge QD heteroepitaxy with the integration in CMOS sensors, some issues must be addressed. Ge/Si growth imposes a hard constraint in all the phases, mostly in surface cleaning. QD deposition should be one of the latest steps, to prevent QDs arrays to be destroyed by any following high temperature process. Likewise, in the formation of the dots high temperatures should be avoided, to protect the underlying circuitry. Therefore, temperatures lower than 450°C are required. In [42],

[6] Magnetron sputtering is technique based on bombarding a surface with high energy ions, which are guided to the target by a magnetic field. More information available in http://www.semicore.com/news/92-what-is-rf-sputtering.

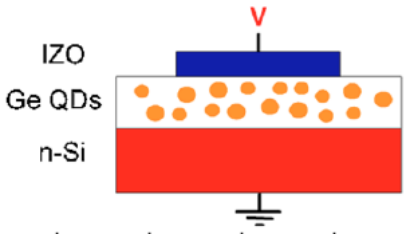

Figure 3.22: Schematic view of a Ge QDPD on a silicon substrate [5].

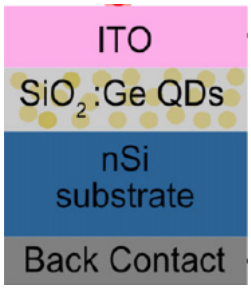

Figure 3.23: Schematic view of a Ge QDPD on a silicon substrate [32].

a hydrogenation technique using hydrogen fluoride (HF) is proposed, achieving surface preparation temperatures of 470°C, which could be further lowered to 400°C.

A top contact of either ITO or Indium-zinc-oxide (IZO) is sputtered to form the top contact. As it happened with the lead sulphide (PbS) QDPDs, these materials are chosen because of their high transparency in the visible and infrared range. With this treatment, Ge-QDs gap energy is reported to be 1.6 eV, which is a good figure for VIS and even UV (IR wavelengths can be absorbed too, though less efficiently).

QD Performance

A good performance in image sensing has been reported for Ge-based PD. Responsivities can rise as high as 4 A/W, bias of -10 V, and to 1.75 A/W at a lower bias of -2 V. In Fig. 3.24, a diagram of the responsivity at different bias and wavelengths is represented. Responsivities as high as 10 A/W were obtained at -4 V bias, lowering to 1.5 A/W at -2 V. Maximum responsivity is achieved in the 700-800 nm range (red-infrared) for high bias, and is almost constant for a lower -2 V. Average silicon detector's responsivities range from 0.4 to 2.8 A/W, so values obtained with Ge QDs seriously challenge current available technologies.

Another figure of merit is the Internal Quantum Efficiency (IQE). High values are obtained, rising to 700% (-10 V bias) or 300% (-2 V bias) [5], and to 1700% (-4 V bias)

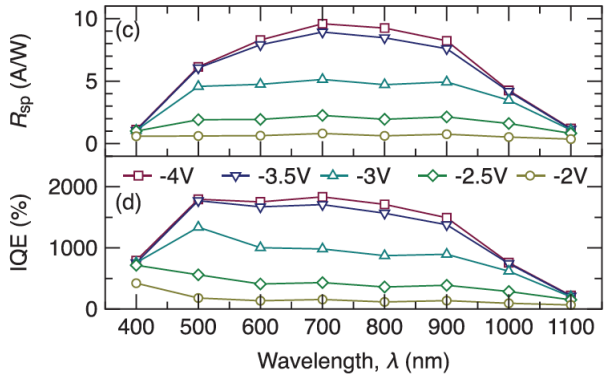

Figure 3.24: Responsivity and IQE depending on the wavelength

or 400% (-2 V bias). However, these are peak values; a more detailed image of how IQE changes with incident wavelength and reverse bias is given in Fig. 3.24. An explanation for this high photoconductive gain needs an insight on the internal behaviour of the charges: electron-hole pairs are generated mostly in the Ge QDs, although the Si substrate contributes too. Due to the difference in the effective mass, holes are heavier than electrons and therefore slower in tunnelling between QDs. This causes a hole accumulation in the Ge QDs layer. To keep charge neutrality, additional electrons have to be supplied from the top contact (IZO, ITO), which tunnel through SiO_2, increasing the total photocurrent. This proves that both the Ge QDs and the Si substrate are fundamental to provide a wide range of absorption.

Transient photoresponse is pretty low compared to PbS QDs; τ_{rise}, τ_{fall} measurements yield values below 35 ns [32], although the experiment protocol was not the same, so results cannot be directly compared. In any case, the response is fast enough for high-speed devices.

Chapter 4

Conclusions

Insights on QDs state of the art have been provided in Chapter 2, with a focus on fabrication and modelling of their optoelectronic properties. Many theoretical models have been developed since the 90s, being the one proposed in this work one of the latest, based on 8kp method, which has proved to yield the most accurate results. However, any practical use of the dots must be adjusted with experimental data: size and shape can be determined with microscopy techniques (AFM, TEM, for instance), whereas the electronic structure landscape can be determined using transmission and absorption spectroscopy [13].

Regarding Chapter 3, a brief introduction on currently available photodetectors has been given, to compare its structure with the QDPD studied later. As it has been explained, the most developed technology are PbS QDPDs, since many more scientific publications have been published using this material. PbS based photodetectors are in a much more advanced state of the art, with sensors already commercialized [36]. Fig. 4.1 and Fig. 4.2 show two examples of pictures taken with a PbS QD-based camera, the *Acuros CQD 640/640L GigE SWIR Camera* developed by *Swir Vision Systems*.

Despite of all the advances, some issues must still be addressed: improve detectivity, achieve lower thermal noise, improve the resolution and reduce their cost to the level of Si-based sensors. Another problem not mentioned yet is toxicity; in general, it is most likely to see small bandgap transitions in heavy metals (Pb, Hg, e.g.), which have the problem of being toxic. According to the WHO [25], lead is "a cumulative toxicant that affects multiple body systems". In very small quantities and well isolated from the environment, there should be no risk at all. Nevertheless, a risk of exposure might arise

Figure 4.1: Image through a maritime rain event. Picture taken with the *Acuros CQD 640/640L GigE SWIR Camera* [36].

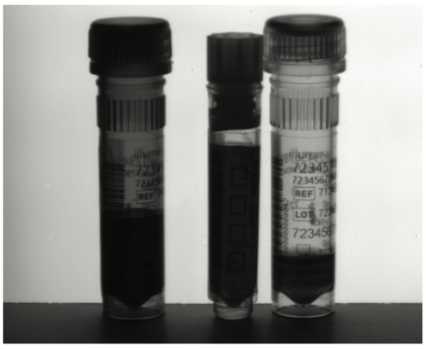

Figure 4.2: Pharmaceutical via labels. Picture taken with the *Acuros CQD 640/640L GigE SWIR Camera* [36].

in manufacturing and recycling process; this must be accounted and properly prevented.

Germanium QDs are presented as a very promising alternative to both InGaAs and PbS detectors, due the good figures of reference presented before. Although of great interest, Ge based QDPDs have not reached yet to a technological readiness level to deem them as an alternative for current available sensors. Most recent research has only been focused on analysing their optoelectronic properties, but a proof-of-concept prototype used as a real camera still lacks. Also, they have shown a better behaviour in the visible than in the infrared; superseding Si PD seems difficult in terms of cost-performance in the short-medium term. Despite of this, the advantages of QDs and the possibility of building multispectral photodetectors justify further research.

It can be concluded that QDPD still have a long way to go before they become of common use in photodetection. Increasing demand of IR sensors might boost research, so in the next years more and more cameras may integrate this quantum technology.

Bibliography

[1] Antonio Arnau and David Soares. "Fundamentals on Piezoelectricity". In: *Piezoelectric Transducers and Applications*. Ed. by Antonio Arnau Vives. Berlin, Heidelberg: Springer Berlin Heidelberg, 2004, pp. 1–37. ISBN: 978-3-662-05361-4. DOI: 10.1007/978-3-662-05361-4_1. URL: https://doi.org/10.1007/978-3-662-05361-4_1.

[2] Ralph Baierlein. "Thermal Physics". In: Cambridge, U.K. ; New York : Cambridge University Press, 1999. ISBN: 978-0521658386.

[3] Elena Borovitskaya and Michael S Shur. *Quantum Dots*. WORLD SCIENTIFIC, 2002. DOI: 10.1142/4934. eprint: https://www.worldscientific.com/doi/pdf/10.1142/4934. URL: https://www.worldscientific.com/doi/abs/10.1142/4934.

[4] Gaoqi Cao et al. "Multicolor Broadband and Fast Photodetector Based on InGaAs Insulator–Graphene Hybrid Heterostructure". In: *Advanced Electronic Materials* 6.3 (), p. 1901007. DOI: https://doi.org/10.1002/aelm.201901007. eprint: https://onlinelibrary.wiley.com/doi/pdf/10.1002/aelm.201901007. URL: https://onlinelibrary.wiley.com/doi/abs/10.1002/aelm.201901007.

[5] S. Cosentino et al. "High-efficiency silicon-compatible photodetectors based on Ge quantum dots". In: *Applied Physics Letters* 98.22 (2011), p. 221107. DOI: 10.1063/1.3597360. eprint: https://doi.org/10.1063/1.3597360. URL: https://doi.org/10.1063/1.3597360.

[6] Yole Développment. *CMOS Image Sensor (CIS) Industry*. URL: http://www.yole.fr/CMOS_Image_Sensors_Industry_Overview.aspx.

[7] Eric R. Fossum and Donald B. Hondongwa. "A Review of the Pinned Photodiode for CCD and CMOS Image Sensors". In: *IEEE Journal of the Electron Devices Society* 2.3 (2014), pp. 33–43. DOI: 10.1109/JEDS.2014.2306412.

[8] Epimitheas Georgitzikis et al. “Integration of PbS Quantum Dot Photodiodes on Silicon for NIR Imaging”. In: *IEEE Sensors Journal* 20.13 (2020), pp. 6841–6848. DOI: 10.1109/JSEN.2019.2933741.

[9] David J. Griffiths and Darrell F. Schroeter. *Introduction to Quantum Mechanics*. 3rd ed. Cambridge University Press, 2018. DOI: 10.1017/9781316995433.

[10] Chen Hu et al. “The micropatterning of layers of colloidal quantum dots with inorganic ligands using selective wet etching”. In: *Nanotechnology* 25.17 (Apr. 2014), p. 175302. DOI: 10.1088/0957-4484/25/17/175302. URL: https://doi.org/10.1088/0957-4484/25/17/175302.

[11] Icinsights. *CMOS Image Sensor Sales Stay on Record-Breaking Pace*. URL: https://www.icinsights.com/news/bulletins/CMOS-Image-Sensor-Sales-Stay-On-RecordBreaking-Pace/.

[12] Hongtao Jiang and J. Singh. “Self-assembled semiconductor structures: electronic and optoelectronic properties”. In: *IEEE Journal of Quantum Electronics* 34.7 (1998), pp. 1188–1196. DOI: 10.1109/3.687862.

[13] Hongtao Jiang and Jasprit Singh. “Conduction band spectra in self-assembled InAs/GaAs dots: A comparison of effective mass and an eight-band approach”. In: *Applied Physics Letters* 71.22 (1997), pp. 3239–3241. DOI: 10.1063/1.120302. eprint: https://doi.org/10.1063/1.120302. URL: https://doi.org/10.1063/1.120302.

[14] Richard G Jones et al., eds. *Compendium of Polymer Terminology and Nomenclature. IUPAC Recommendations 2008*. The Royal Society of Chemistry, 2009, P001–443. ISBN: 978-0-85404-491-7. DOI: 10.1039/9781847559425. URL: http://dx.doi.org/10.1039/9781847559425.

[15] Yeongho Kim et al. “Effect of spacer layer thickness on structural and optical properties of multi-stack InAs/GaAsSb quantum dots”. In: *Applied Physics Letters* 107.17 (2015), p. 173109. DOI: 10.1063/1.4934695. eprint: https://doi.org/10.1063/1.4934695. URL: https://doi.org/10.1063/1.4934695.

[16] Petr Klenovský, Andrei Schliwa, and Dieter Bimberg. “Electronic states of (InGa)(AsSb)/GaAs/GaP quantum dots”. In: *Physical Review B* 100.11 (Sept. 2019). ISSN: 2469-

9969. DOI: 10.1103/physrevb.100.115424. URL: http://dx.doi.org/10.1103/PhysRevB.100.115424.

[17] Gerasimos Konstantatos. "Colloidal quantum dot photodetectors". In: *Colloidal Quantum Dot Optoelectronics and Photovoltaics*. Ed. by Gerasimos Konstantatos and Edward H.Editors Sargent. Cambridge University Press, 2013, pp. 173–198. DOI: 10.1017/CBO9781139022750.008.

[18] Michael Kriss. *Handbook of Digital Imaging*. John Wiley Sons, Ltd., 2015. Chap. 3. ISBN: 978-0-470-51059-9.

[19] M. H. Kuo et al. "Designer Ge quantum dots on Si: A heterostructure configuration with enhanced optoelectronic performance". In: *Applied Physics Letters* 101.22 (2012), p. 223107. DOI: 10.1063/1.4768292. eprint: https://doi.org/10.1063/1.4768292. URL: https://doi.org/10.1063/1.4768292.

[20] E.M.Lifschitz L.D.Landau. *Mecánica, volumen 1, Curso de Física Teórica*. Editorial Reverté, 1994.

[21] Olga L. Lazarenkova and Alexander A. Balandin. "Miniband formation in a quantum dot crystal". In: *Journal of Applied Physics* 89.10 (2001), pp. 5509–5515. DOI: 10.1063/1.1366662. eprint: https://doi.org/10.1063/1.1366662.

[22] Clément Livache et al. "Road Map for Nanocrystal Based Infrared Photodetectors". In: *Frontiers in Chemistry* 6 (2018), p. 575. ISSN: 2296-2646. DOI: 10.3389/fchem.2018.00575. URL: https://www.frontiersin.org/article/10.3389/fchem.2018.00575.

[23] Pawel E. Malinowski et al. "Thin-Film Quantum Dot Photodiode for Monolithic Infrared Image Sensors". In: *Sensors* 17.12 (2017). ISSN: 1424-8220. URL: https://www.mdpi.com/1424-8220/17/12/2867.

[24] nanoHUB.org. *On-line Simulation and More for Nanotechnology*. URL: http://nanoHUB.org.

[25] World Health Organisation. *Lead Poisoning and Health*. URL: https://www.who.int/news-room/fact-sheets/detail/lead-poisoning-and-health.

[26] Onur Özdemir et al. “High Sensitivity Hybrid PbS CQD - TMDC Photodetectors up to 2 m”. In: *ACS Photonics* 2019 (Sept. 2019). DOI: 10.1021/acsphotonics.9b00870.

[27] Dr. Rüdiger Paschotta. *Responsivity*. URL: https://www.rp-photonics.com/responsivity.html.

[28] Antoni Rogalski. “Infrared detectors: status and trends”. In: *Progress in Quantum Electronics* 27.2 (2003), pp. 59–210. ISSN: 0079-6727. DOI: https://doi.org/10.1016/S0079-6727(02)00024-1. URL: https://www.sciencedirect.com/science/article/pii/S0079672702000241.

[29] Samsung. *QLED TV*. URL: https://www.samsung.com/uk/tvs/tv-buying-guide/what-is-qled-tv/.

[30] Andrei Schliwa and Momme Winkelnkemper. “Theory of Excitons in InGaAs/GaAs Quantum Dots”. In: *Semiconductor Nanostructures*. Ed. by Dieter Bimberg. Berlin, Heidelberg: Springer Berlin Heidelberg, 2008, pp. 139–164. ISBN: 978-3-540-77899-8. DOI: 10.1007/978-3-540-77899-8_7. URL: https://doi.org/10.1007/978-3-540-77899-8_7.

[31] L. E. Scriven. “Physics and Applications of DIP Coating and Spin Coating”. In: *MRS Proceedings* 121 (1988), p. 717. DOI: 10.1557/PROC-121-717.

[32] S. Shi, A. Zaslavsky, and D. Pacifici. “High-performance germanium quantum dot photodetectors: Response to continuous wave and pulsed excitation”. In: *Applied Physics Letters* 117.25 (2020), p. 251105. DOI: 10.1063/5.0025660. eprint: https://doi.org/10.1063/5.0025660. URL: https://doi.org/10.1063/5.0025660.

[33] Siltronix. *Silicon wafer specifications*. URL: https://www.sil-tronix-st.com/en/silicon-wafer/silicon-wafer-specifications.

[34] Jasprit Singh. *Electronic and Optoelectronic Properties of Semiconductor Structures*. Cambridge University Press, 2003. DOI: 10.1017/CBO9780511805745.

[35] Rafal Sliz et al. “Stable Colloidal Quantum Dot Inks Enable Inkjet-Printed High-Sensitivity Infrared Photodetectors”. In: *ACS Nano* 13.10 (2019). PMID: 31545597, pp. 11988–11995. DOI: 10.1021/acsnano.9b06125. eprint: https://doi.org/10.1021/acsnano.9b06125. URL: https://doi.org/10.1021/acsnano.9b06125.

[36] New Imaging Technologies. *SWIR Products*. URL: https://new-imaging-technologies.com/swir-products/.

[37] Hareesh Tummala. "3D Discrete Dislocation Dynamics simulations of the role of interfaces in confined materials - : application to electronic devices such as LEDs". PhD thesis. Dec. 2016.

[38] Irene Tzinis. *Technology Readiness Level*. URL: https://www.nasa.gov/directorates/heo/scan/engineering/technology/technology_readiness_level.

[39] I-Hsiang Wang et al. "The Wonderful World of Designer Ge Quantum Dots". In: *2020 IEEE International Electron Devices Meeting (IEDM)*. 2020, pp. 38.1.1–38.1.4. DOI: 10.1109/IEDM13553.2020.9372027.

[40] A. I. Yakimov et al. "Surface plasmon dispersion in a mid-infrared Ge/Si quantum dot photodetector coupled with a perforated gold metasurface". In: *Applied Physics Letters* 112.17 (2018), p. 171107. DOI: 10.1063/1.5029289. eprint: https://doi.org/10.1063/1.5029289. URL: https://doi.org/10.1063/1.5029289.

[41] Peter Y. Yu and Manuel Cardona. "Electronic Band Structures". In: *Fundamentals of Semiconductors: Physics and Materials Properties*. Berlin, Heidelberg: Springer Berlin Heidelberg, 2010, pp. 17–106. ISBN: 978-3-642-00710-1. DOI: 10.1007/978-3-642-00710-1_2. URL: https://doi.org/10.1007/978-3-642-00710-1_2.

[42] Vladimir Yuryev and Larisa Arapkina. "Ge quantum dot arrays grown by ultrahigh vacuum molecular-beam epitaxy on the Si(001) surface: Nucleation, morphology, and CMOS compatibility". In: *Nanoscale research letters* 6 (Sept. 2011), p. 522. DOI: 10.1186/1556-276X-6-522.

Appendix A

Image Sensor Parameters

-Quantum Efficiency (QE, η): it is defined as the "average number of electron-hole pairs collected by a photodetector when one photon enters the pixel" [18]. Basically, it describes how well detector and radiation are coupled. Its formula is

$$QE(\lambda) = \frac{\text{photocarriers}}{\text{incoming photons}} \tag{A.1}$$

Two types can be distinguished, depending on the distinction of the incident photons:

1. Internal Quantum Efficiency (IQE): considers all the photons absorbed by the detector

2. External Quantum Efficiency (EQE): considers all the photons impinging on the photodetector

-Dark current (I_d): "rate at which carriers are collected by the pixel when no illumination is incident on the sensor" [18]. It is usually measured in nA or pA.

-Gain (G): number of carriers passing contacts per one generated pair. It is a measure of how well electron-hole pairs are converted into photocurrent. It is assumed to be constant over the volume of the device.

-Responsivity (R): ratio between the photocurrent and the flux of incident light. Usually measured in amperes per watt (A/W). It is the ability of the active layer to transform light into an electrical signal [22]. It is obtained from the quantum efficiency(η) [27]:

$$R = \eta \frac{q}{h\nu} \tag{A.2}$$

where $h\nu$ is the incident photon energy and q the charge of the carrier.

-Detectivity (D*): main parameter characterizing normalized to signal noise performance of detectors; it measures the signal to noise ratio produced by a $1cm^2$ detector when 1W of optical power impinges on it, measured with an electrical bandwidth of 1Hz. Its main advantage is that it allows to compare the performance of detectors with different sizes and geometries. Values are given in units of $\text{cm} \cdot \text{Hz}^{1/2}\text{W}^{-1}$ or in jones (1 Jones=1 $\text{cm} \cdot \text{Hz}^{1/2}\text{W}^{-1}$).

Assuming that the dark current is the main source of noise, Detectivity can be related to responsivity as follows [8]:

$$D^* = RA^{1/2}(2qI_d)^{-1/2} \tag{A.3}$$

where R is the responsivity and A the surface area.

-Temporal photoresponse: time taken to rise to $1 - 1/e$ (τ_{rise}) and fall to $1/e$ (τ_{fall}) in a peak value, after an excitation of the system with light [8]. Also called transient time.

Appendix B

Image Sensor Technologies

The two main underlying technologies of image sensors, as it has been pointed in Chapter 3, are CCDs and CMOSs. A brief explanation of their working principles will be provided here. A more detailed review on this topic may be found in [18].

B.0.1 Charge Coupled Devices (CCDs)

Their operation principle is based on a MOS capacitor (a device designed to store charge). The voltage on the gate of this capacitor creates a potential well, which can be used to store charges. In the case of the sensor, by controlling the voltages on each gate of pixel, a potential profile can be created. Voltage differences also allow to move the charges from the left to the right, that is, from pixel to pixel. Thus, photocharge is moved from the pixel where light is "harvested" down to the vertical CCD and then to the horizontal CCD. From there, photocharge is carried to an output amplifier and the signal is interpreted by the software.

The main advantage of CCDs is their ability to transport charges almost noisily. However, to fulfil this characteristic, the transfer process has to be almost perfect. Their use has decreased to the benefit of CMOSs.

B.0.2 Complementary-Metal-Oxide-Semiconductor (CMOS)

CMOSs image sensors are formed by an array of pixels, row and column decoders, column amplifiers and output multiplexer. They can be either active or passive pixel sensors. Almost all the sensors currently designed are based on the active ones, so only the working

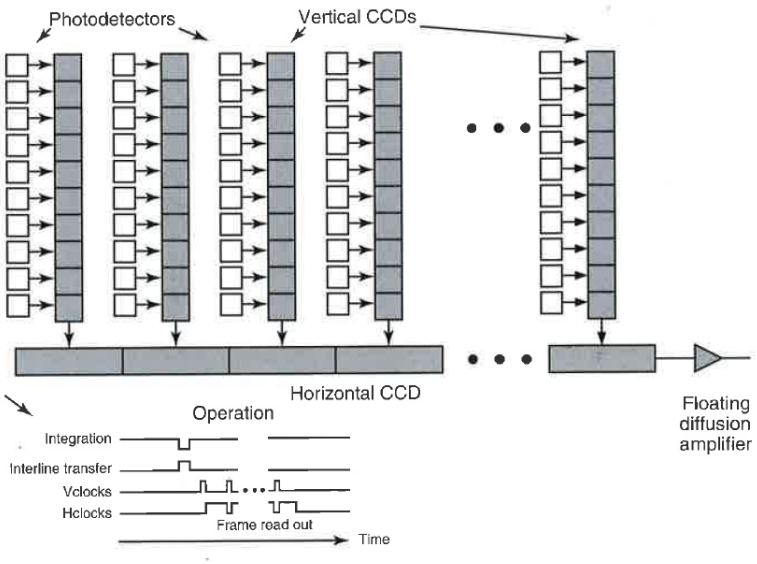

Figure B.1: Diagram of CCD image sensor [18].

principle of these will be described.

Three different parts can be identified: the storage well (SW), the transfer gate (TG) and the floating device (FD), an output contact. Signal photocarriers are collected and stored in SW (QDs in this thesis), while keeping them well isolated from FD by a low voltage. FD is reset and, by changing the potential of TG, the charge is transferred from SW to FD, to be afterwards analysed.

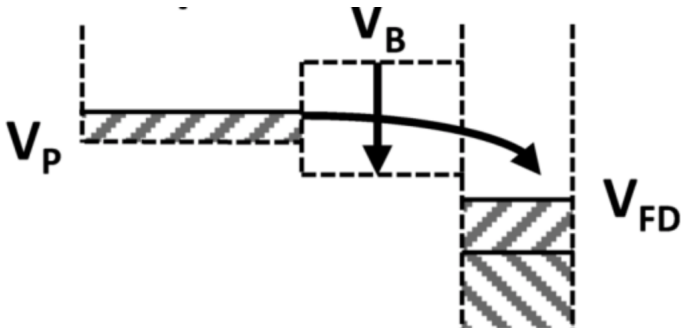

Figure B.2: Potential profile, ilustrating the action of the transfer gate (TG) [7].